Arctic rift system driven by a giant stagnant slab

Genti Toyokuni[1] and Dapeng Zhao[1]

[1]Tohoku University

November 23, 2022

Abstract

A detailed 3-D tomographic model of the whole mantle beneath the circum-Arctic region is obtained by applying an updated global tomography method to a large amount of P-wave arrival time data. Our model clearly shows the subducted Izanagi and Farallon slabs penetrating into the lower mantle beneath Eurasia and North America, respectively. In the region from Canada to Greenland, a giant stagnant slab lying below the 660-km discontinuity is revealed. Because this slab has a texture that seems to be due to subducted oceanic ridges, the slab might be composed of the Izanagi, Farallon, Kula and Vancouver slabs that had subducted during ˜80-20 Ma. During that period, a complex rift system represented by division between Canada and Greenland was developed. The oceanic ridge subduction and hot upwelling in the big mantle wedge above the stagnant slab caused a tensional stress field, which might have induced these complex tectonic events.

Arctic rift system driven by a giant stagnant slab

Genti Toyokuni[1*] and Dapeng Zhao[1]

[1] Department of Geophysics, Graduate School of Science, Tohoku University, Sendai 980-8578, Japan

Submitted to ***Geophysical Research Letters*** in June 2021

*Corresponding author:

Genti Toyokuni

E-mail: toyokuni@tohoku.ac.jp

ORCID ID: 0000-0003-3786-207X

Key Points:

- High-resolution *P* wave tomography of the whole mantle beneath the circum-Arctic region is obtained.
- A giant stagnant slab with subducted oceanic ridge is revealed below the 660-km discontinuity beneath Canada and Greenland.
- Division between Canada and Greenland at 63−35 Ma might be induced by complex tensional field associated with the stagnant slab.

Abstract

A detailed 3-D tomographic model of the whole mantle beneath the circum-Arctic region is obtained by applying an updated global tomography method to a large amount of *P*-wave arrival time data. Our model clearly shows the subducted Izanagi and Farallon slabs penetrating into the lower mantle beneath Eurasia and North America, respectively. In the region from Canada to Greenland, a giant stagnant slab lying below the 660-km discontinuity is revealed. Because this slab has a texture that seems to be due to subducted oceanic ridges, the slab might be composed of the Izanagi, Farallon, Kula and Vancouver slabs that had subducted during ~80−20 Ma. During that period, a complex rift system represented by division between Canada and Greenland was developed. The oceanic ridge subduction and hot upwelling in the big mantle wedge above the stagnant slab caused a tensional stress field, which might have induced these complex tectonic events.

Plain Language Summary

The circum-Arctic region has many clues for understanding global-scale tectonics and revolution of the Earth. Seismic tomography is a well-established method for obtaining 3-D images of the underground structure by inverting a large number of seismic wave arrival times. We obtain detailed tomographic images of the whole mantle beneath the circum-Arctic region by using an updated global tomography method. Our high-resolution results clearly show the subducted Izanagi and Farallon slabs penetrating into the lower mantle beneath Eurasia and North America, respectively. In the region from Canada to Greenland, a giant stagnant slab lying below the 660-km discontinuity with a total length of ~4,000 km is revealed. Because this slab has a texture that seems to be due to subducted oceanic ridges, the slab might be composed of the Izanagi, Farallon, Kula and Vancouver slabs that had subducted during ~80−20 Ma. During that period, a complex rift system represented by division between Canada and Greenland was developed. The oceanic ridge subduction and hot upwelling in the big mantle wedge above the stagnant slab caused a tensional stress field, which might have induced these complex tectonic events.

1. Introduction

The underground structure beneath the circum-Arctic region (Figure 1) is a frontier of our geoscientific knowledge that has been poorly understood compared to other regions of the Northern Hemisphere. Especially in recent years, the underground structure and tectonics of this area have received widespread attention because, for example, a possibility of resource mining has increased due to decrease in ice in the Arctic Ocean, and the underground temperature affects melting of the Greenland Ice Sheet and global sea level rise (Martos et al., 2018; Toyokuni et al., 2020a).

One of the major mysteries of tectonics in this area is the existence of the Canadian Arctic Rift System (CARS). Its latest activity was the Eurekan Rifting Episode (ERE), symbolized by the division between Greenland and Canada and complex movement of the Canadian Arctic Archipelago (CAA), which took place between 63 and 35 Ma (Gion et al., 2017). It is known that this division began in the Labrador Sea on the south side and propagated to Baffin Bay on the north side. Simultaneously, flood basalts erupted widely in West Greenland, Davis Strait, and Baffin Island (Chalmers et al., 1995; Larsen et al., 2016). Traditionally, these events were thought to be induced by the rising Iceland plume (Gerlings et al., 2009; Gill et al., 1992). However, from reconstruction of the plume track (Peace et al., 2017), geothermal heat flow estimation (Artemieva, 2019; Martos et al., 2018), and seismic velocity structure (Toyokuni et al., 2020a), it is unlikely that the Iceland plume passed through this area. Peace et al. (2017)

proposed a far field tectonic force as an alternative mechanism that caused the division, but they did not mention its direct cause.

In Greenland, a seismograph network had recently been developed with international cooperation, and high-quality data have been accumulated (Clinton et al., 2014; Toyokuni et al., 2014). Structures beneath Greenland, Iceland, and surrounding regions have been intensively investigated by seismic waveform analyses (Kumar et al., 2007; Mordret et al., 2016; Toyokuni et al., 2015, 2018, 2021a), surface wave tomography (Antonijevic & Lees, 2018; Darbyshire et al., 2004, 2018; Levshin et al., 2017; Mordret, 2018; Pilidou et al., 2004; Pourpoint et al., 2018), body wave tomography (Toyokuni & Zhao, 2021; Toyokuni et al., 2020a, 2020b), and full-wave tomography (Rickers et al., 2013). However, the previous studies targeting the whole circum-Arctic region focused on the structure shallower than 700 km depth (Jakovlev et al., 2012; Lebedev et al., 2017). Seismic tomography, especially body-wave tomography, is a well-established and high-resolution method for investigating deep structure of the Earth. To investigate the relationship between tectonics of the circum-Arctic region and large-scale geodynamic events such as plate subduction and hot mantle plume that occurred or are occurring in surrounding regions, we need to study the whole mantle structure with high resolution over a vast horizontal scale. In this study we exploit the updated global tomography method that can reveal the whole mantle structure beneath a specific area with high resolution (Toyokuni et al., 2020b; Zhao et al., 2017) to execute multiple computations for different areas, and to obtain detailed panoramic tomography by stitching the individual images together. The purpose of this study is to investigate the cause of ERE from a tectonic viewpoint using our novel tomographic model.

2. Data & Method

We apply the multiscale global tomography method by Zhao et al. (2017), which adopts a fine 3-D grid for the target region and a coarse 3-D grid for the surrounding regions of the globe. Thus, the structural model beneath the target region can be obtained with high resolution while saving computational resources. Applying this method to the Izu-Bonin subduction zone, Zhao et al. (2017) investigated the detailed 3-D structure of the subducted Pacific slab where the 2015 Bonin deep earthquake (*M*7.9; depth ~ 680 km) took place. This method was also applied to investigate the whole mantle structure beneath Greenland (Toyokuni et al., 2020b) and Southeast Asia (Zhao et al., 2021).

We apply a coordinate transformation that moves the center of the target area to (longitude, latitude) = (90°, 0°) to treat high latitude areas by nearly rectangular grid distributions (Takenaka et al., 2017; Toyokuni et al., 2020a, 2020b). To clarify the relationship between tectonic phenomena with a large horizontal scale such as plate subduction and a hot mantle plume, our target covers the entire region north of ~30°N latitude. The computation cost is reduced by performing independent calculations with 12 different regions and superimposing the results to obtain a final tomographic model.

Table S1 shows the central location (longitude and latitude) for each of the 12 regions. Each calculation is performed for a region covering the longitude range from 60° to 120° and the latitude range from −30° to 30° after the coordinate transformation. In the vicinity of the North Pole, where only a few seismic stations and earthquakes exist, calculations are performed in two regions rotated by ~40° around the North Pole to reduce the distortion of the results due to the grid arrangement (Regions 1 and 2). In addition, 10 regions with different positions and angles are further arranged around them (Regions 3−12) (Figure S1).

Data are collected from the ISC-EHB catalog at the International Seismological Centre (ISC) website (http://www.isc.ac.uk/) and further selected for our analysis. The *P*, *pP*, and *PP* (Figure S2) arrival times from 170,435 earthquakes are selected. To make the hypocentral distribution uniform, the entire crust and mantle are divided into small cubic blocks, and only one earthquake with the largest number of data in each block is extracted. We extract as many earthquakes as possible that occurred inside the target region, by adopting finer blocks inside the target region and coarser blocks outside it. The block size is changed for each calculation to roughly homogenize the number of earthquakes and data used in each calculation (Table S1 and Figures S3−S14). Table S1 also shows the numbers of seismic stations and arrival time data used.

We set a fine 3-D grid with a lateral grid interval of 55.6 km (a great circle distance of 0.5° on the surface) in the target region, and a coarse 3-D grid with a lateral grid interval of 222.39 km (a great circle distance of 2.0° on the surface) outside the target region. The vertical grid intervals inside and outside the target region are also different (see Table S2). Theoretical traveltimes are calculated using a 3-D ray tracing method (Zhao, 2004) that simultaneously uses the pseudo-bending scheme (Um & Thurber, 1987) and Snell's law. The IASP91 model (Kennett & Engdahl, 1991) is taken to be the 1-D initial Vp model for the tomographic inversion (Figure S15). The tomographic inversion is conducted using the LSQR algorithm (Paige & Saunders, 1982) with damping and smoothing regularizations (Zhao, 2004). The optimal values of the damping and smoothing parameters are adopted according to the previous studies (Toyokuni et al., 2020b; Zhao et al., 2017, 2021).

To reduce the influence of boundary of the target region, the edges of each tomographic model obtained by the individual inversion for the 12 regions are cut off, and we extract only the results 4° inside the longitude and latitude ranges of the target region. Then we rearrange the 12

Vp models according to the coordinate system of Region 1, and take weight average using the ray hit count. As a result, the final tomographic model is obtained from the surface to the core-mantle boundary (CMB) beneath the region north of ~30°N latitude. Such jointing of multiple tomography results has been adopted by previous studies targeting a wide area (e.g., Jakovlev et al., 2012).

3. Results

Map view images of the tomographic results are shown in Figures 2 and S16. For the areas where some of the 12 regions overlap, the ray hit count (HC) in each region is averaged, and the regions where average HC < 20 (Figure S17) are masked in white. At a depth of 160 km, high-Vp anomalies are visible in forearc regions, and low-Vp and high-Vp anomalies appear in the eastern and western parts of North America, respectively, which is consistent with previous tomographic models (e.g., Golos et al., 2018). At a depth of 400 km, a low-Vp zone beneath the Iceland and Azores hotspots is visible. At a depth of 800 km, a wide range of high-Vp from North America to North Eurasia and low-Vp in surrounding regions are prominent. At a depth of 1500 km, no distinctive features are visible, but at a depth of 2100 km, the "Greenland plume" (Toyokuni et al., 2020b) and low-Vp beneath the western Pacific are prominent. At a depth of 2880 km, there is a marked increase in high-Vp and low-Vp amplitudes near CMB.

Vertical cross-sections of our model (Figure 3) clearly image the subducting Farallon slab beneath the North American continent, which has penetrated into the lower mantle (Figure 3a). Beneath the Eurasian continent, the Izanagi slab penetrating into the lower mantle is also clearly resolved (Figure 3c). As a plate becomes thicker and heavier as it moves away from the ridge axis, it is likely to fall into the lower mantle after stagnation around the 660-km discontinuity. The penetration of the Farallon slab into the lower mantle has already been revealed by many tomographic studies (e.g., Schmid et al., 2002; Zhao, 2004). On the other hand, penetration of the Izanagi slab was only predicted by studies based on mantle convection modeling (Peng & Liu, 2021). This is the first time that the penetrating Izanagi slab is clearly imaged by seismic tomography. In Figure 3a, we can also see low-Vp, which appears to be a hot plume rising from the CMB below Hawaii toward the west coast of North America.

Beneath Canada and Greenland, located between the two penetrating slabs, a high-Vp anomaly lies at depths of ~800 km (Figure 3b). While this high-Vp anomaly can be seen almost near the surface at the western end, it deepens toward the east and continues for a total length of ~4,000 km. This feature reminds us of a giant stagnant slab. Vertical cross-sections with a finer grid interval beneath Canada and Greenland are shown in Figure S18. Comparisons with other tomographic models (Amaru, 2007; Lu et al., 2019; Ritsema et al., 2011; Simmons et al., 2010, 2012) show that the main features in Figure 3a are robust, but those in Figures 3b and 3c vary depending on the model (Figures S19−S21).

The resolution of the tomographic images is investigated using multiple synthetic tests including the checkerboard resolution test (CRT) (Humphreys & Clayton, 1988; Zhao et al., 2017) and restoring resolution test (RRT) (Toyokuni et al., 2021b; Zhao et al., 2017). Specifically, the following four input Vp models are constructed and tested (Toyokuni et al., 2020b): (1) CRT1: the checkerboard has a lateral grid interval of 278 km (a great circle distance of 2.5° on the surface) inside the study region, (2) CRT2: the lateral grid interval is 167 km (a great circle distance of 1.5° on the surface) inside the study region, (3) RRT1: highlighting the pattern of the obtained tomographic result, (4) RRT2: the same as RRT1 but a regional rectangular high-Vp anomaly is added at depths of 650-800 km. Figures S22−S25 show the recovery rate of CRT (Toyokuni et al., 2020b) and the RRT results. The CRT results show that the resolution in our study region is 1.5° in the lateral direction and the distances comparable to the vertical grid interval in the depth direction for regions with average HC ≥ 20. The RRT results also show that the pattern of tomographic results can be recovered very well. Figures S26−S28 also show the reliability of main features in Figure 3.

4. Discussion

The map view at a depth of 800 km (Figures 2c and 4a) shows that the amplitude of high-Vp anomalies in the region from Canada to the Arctic Ocean is not uniform, and that the amplitude changes like stripes. Comparison of RRT1 and RRT2 results indicates that this feature is reliable (Figure S29). Overlapping the results of plate reconstruction by Müller et al. (2019), these stripes are coincident with the oceanic ridge axis subducted approximately normal to the trench axis. Specifically, the regions with the lineament of weaker high-Vp amplitudes are consistent well with the ridge axis between the Farallon and Izanagi plates subducted during 160−85 Ma, and the ridge axis at the boundary of the Kula and Vancouver plates subducted during 85−20 Ma (Figure 4 and Video S1). Therefore, we consider that the lineament of weak high-Vp anomalies indicates the subducted oceanic ridge where the slab is thin, and the lineament with strong high-Vp zones on its both sides indicates the part where the slabs are relatively thick. This correspondence reinforces the possibility that the high-Vp anomaly beneath this region reflects a stagnant slab.

According to a recent study (Domeier et al., 2017), the traditionally considered Kula plate is a complex of the western Kronos plate and the eastern Kula plate, with subduction of the Kula plate beneath the Kronos plate forming a westward slope. In this case, the subduction axis of the Kula plate runs almost parallel to the eastern Kula−Farallon ridge, which better corresponds to the two parallel lineaments of weak high-Vp zones beneath North America in our tomographic results.

The plate near the ridge axis is young and less heavy, so it is easy to stagnant at a depth in the mantle. Furthermore, the trench axis due to the subduction of this area continued to retreat (Figure 4), providing an environment where the slab stagnation was likely to occur. When the slab is light enough, it does not fall into the lower mantle but keeps to stagnate until it is thermally assimilated with its surroundings (Nakakuki et al., 2010).

Above the long stagnant slab, a huge wedge-shaped mantle is formed, which is called the Big Mantle Wedge (BMW) and was firstly found in East Asia (Zhao, 2004; Lei & Zhao, 2005; Zhao et al., 2009). In the BMW, subduction-driven corner flow and fluids from deep dehydration reactions of the stagnant Pacific slab in the mantle transition zone result in upwelling of hot and wet asthenospheric materials, causing intraplate volcanism and continental rift systems in East Asia. The BMW above the subducted Farallon/Nazca slab also caused Cenozoic intraplate magmatism in Patagonia (Navarrete et al., 2020). Referring to these previous studies, combining our tomography and the plate reconstruction results, we propose that the BMW above the stagnant slab in the circum-Arctic region caused the continental breakup during ERE and the accompanying volcanism in West Greenland, Davis Strait, and Baffin Island in Tertiary.

Unlike East Asia and Patagonia, the stagnant slab in the present study region is characterized by the oceanic ridge axis subducted nearly orthogonal to the trench axis. Because the oceanic plates diverge to both sides of the ridge axis, when the ridge is subducted, a tensional stress field is likely to form in the trench-parallel direction in the overlying plate. Combined with the dominant trench-normal tensional stress regime formed by upwelling flows in the BMW, the upper plate in this area is likely to be dominated by tensional stresses oriented in various directions, which might have induced the complex division of CAA (Figure 5).

The root of this stagnant slab is located between the Cascadia and Alaska subduction zones in North America, where currently only the strike-slip Queen Charlotte Fault exists, and the subduction has already ceased. After the ERE, CARS became inactive and the entire rift system is now moving as part of the North American Plate. This fact also supports our proposal that CARS was induced by the stagnant slab. Toyokuni et al. (2020b) discovered the Greenland plume ascending from CMB beneath Greenland, which rises up eastward and is connected with Svalbard and Jan Mayen. The direction of plume fluttering is opposite to the moving direction of the plate on which Greenland is placed. However, considering that the stagnant slab may obstruct the upwelling flow, the strange flowline of the Greenland plume (Toyokuni et al., 2020b) can be well explained.

Acknowledgments

We are grateful to Drs. Dean Childs, Kevin Nikolaus, Kent Anderson, Masaki Kanao, Yoko Tono, Seiji Tsuboi, Robin Abbott, Kathy Young, Drew Abbott, Silver Williams, Jason Hebert, Tetsuto Himeno, Susan Whitley, Orlando Leone, Akram Mostafanejad, Kirsten Arnell, and other staff members at GLISN, IRIS/PASSCAL, CH2M HILL Polar Services, and Norlandair for their contributions to the field operations in Greenland. This work was partially supported by research grants from Japan Society for the Promotion of Science (Nos. 18K03794, 24403006, 23224012, 19H01996, and 26241010). The GMT (Wessel et al., 2013) and GPlates (Müller et al., 2018) software packages are used in this study. The SubMachine website (https://www.earth.ox.ac.uk/~smachine/cgi/index.php) (Hosseini et al., 2018) is used to generate cross sections of other tomography models. Arrival-time data are downloaded from the ISC

(http://www.isc.ac.uk/). Archiving of data from this study is underway through Zenodo. Currently these data can be seen in Supporting Information for review purposes.

Author contributions

Conceptualization: Genti Toyokuni, Dapeng Zhao

Data curation: Genti Toyokuni

Formal analysis: Genti Toyokuni

Methodology: Genti Toyokuni, Dapeng Zhao

Resources: Genti Toyokuni, Dapeng Zhao

Visualization: Genti Toyokuni

Writing – original draft: Genti Toyokuni

Writing – review & editing: Genti Toyokuni, Dapeng Zhao

References

Amaru, M. L. (2007). Global travel time tomography with 3-D reference models. Doctoral thesis, Utrecht University. https://dspace.library.uu.nl/handle/1874/314949

Antonijevic, S. K., & Lees, J. M. (2018). Effects of the Iceland plume on Greenland's lithosphere: New insights from ambient noise tomography. *Polar Science*, 17, 75–82. https://doi.org/10.1016/j.polar.2018.06.004

Artemieva, I. M. (2019). Lithosphere thermal thickness and geothermal heat flux in Greenland from a new thermal isostasy method. *Earth-Science Reviews*, 188, 469–481. https://doi.org/10.1016/j.earscirev.2018.10.015

Chalmers, J. A., Larsen, L. M., & Pedersen, A. K. (1995). Widespread Palaeocene volcanism around the northern North Atlantic and Labrador Sea: evidence for a large, hot, early plume head. *Journal of the Geological Society*, 152, 965–969. https://doi.org/10.1144/GSL.JGS.1995.152.01.14

Clinton, J. F., Nettles, M., Walter, F., Anderson, K., Dahl-Jensen, T., Giardini, D., Govoni, A., Hanka, W., Lasocki, S., Lee, W. S., McCormack, D., Mykkeltveit, S., Stutzmann, E., & Tsuboi, S. (2014). Seismic network in Greenland monitors Earth and ice system. *Eos, Transactions, American Geophysical Union*, 95(2), 13–24. https://doi.org/10.1002/2014EO020001

Darbyshire, F. A., Dahl-Jensen, T., Larsen, T. B., Voss, P. H., & Joyal, G. (2018). Crust and uppermost-mantle structure of Greenland and the Northwest Atlantic from Rayleigh wave group velocity tomography. *Geophysical Journal International*, 212(3), 1546–1569. https://doi.org/10.1093/gji/ggx479

Darbyshire, F. A., Larsen, T. B., Mosegaard, K., Dahl-Jensen, T., Gudmundsson, Ó., Bach, T., et al. (2004). A first detailed look at the Greenland lithosphere and upper mantle, using Rayleigh wave tomography. *Geophysical Journal International*, 158(1), 267–286. https://doi.org/10.1111/j.1365‐246X.2004.02316.x

Domeier, M., Shephard, G. E., Jakob, J., Gaina, C., Doubrovine, P. V., & Torsvik, T. H., (2017). Intraoceanic subduction spanned the Pacific in the Late Cretaceous–Paleocene. *Science Advances*, 3(11), eaao2303. https://doi.org/10.1126/sciadv.aao2303

Gerlings, J., Funck, T., Jackson, H. R., Louden, K. E., & Klingelhöfer, F., 2009. Seismic evidence for plume-derived volcanism during formation of the continental margin in southern Davis Strait and northern Labrador Sea. *Geophysical Journal International*, 176, 980–994. https://doi.org/10.1111/j.1365-246X.2008.04021.x

Gill, R. C. O., Pedersen, A. K., & Larsen, J. G., 1992. Tertiary picrites in West Greenland: melting at the periphery of a plume? In B. C. Storey, T. Alabaster, & R. J. Pankhurst (Eds.), *Magmatism and the Causes of Continental Break-up* (Vol. 68, pp. 335–348). London: Geological Society of London. https://doi.org/10.1144/GSL.SP.1992.068.01.21

Gion, A. M., Williams, S. E., & Müller, R. D. (2017). A reconstruction of the Eurekan Orogeny incorporating deformation constraints, *Tectonics*, 36, 304–320. https://doi.org/10.1002/2015TC004094

Golos, E. M., Fang, H., Yao, H., Zhang, H., Burdick, S., Vernon, F., Schaeffer, A., Lebedev, S., & van der Hilst, R. D. (2018). Shear wave tomography beneath the United States using a joint inversion of surface and body waves. *Journal of Geophysical Research: Solid Earth*, 123, 5169–5189. https://doi.org/10.1029/2017JB014894

Hosseini, K., Matthews, K. J., Sigloch, K., Shephard, G. E., Domeier, M., & Tsekhmistrenko, M. (2018), SubMachine: Web-Based tools for exploring seismic tomography and other models of Earth's deep interior. *Geochemistry, Geophysics, Geosystems*, 19(5), 1464-1483. https://doi.org/10.1029/2018GC007431

Humphreys, E., & Clayton, R. W. (1988). Adaptation of back projection tomography to seismic travel time problems. *Journal of Geophysical Research*, 93(B2), 1073–1085. https://doi.org/10.1029/JB093iB02p01073

Jakovlev, A. V., Bushenkova, N. A., Koulakov, I. Yu., & Dobretsov, N. L. (2012). Structure of the upper mantle in the Circum-Arctic region from regional seismic tomography. *Russian Geology and Geophysics*, 53(10), 963–971. https://doi.org/10.1016/j.rgg.2012.08.001

Kennett, B. L. N., & Engdahl, E. R. (1991). Traveltimes for global earthquake location and phase identification. *Geophysical Journal International*, 105, 429–465. https://doi.org/10.1111/j.1365-246X.1991.tb06724.x

Kumar, P., Kind, R., Priestley, K., & Dahl-Jensen, T. (2007). Crustal structure of Iceland and Greenland from receiver function studies. *Journal of Geophysical Research: Solid Earth*, 112(B3), B03301. https://doi.org/10.1029/2005JB003991

Larsen, L. M., Pedersen, A. K., Tegner, C., Duncan, R. A., Hald, N., & Larsen, J. G. (2016). Age of Tertiary volcanic rocks on the West Greenland continental margin: volcanic evolution and event correlation to other parts of the North Atlantic Igneous Province. *Geological Magazine*, 153, 487–511. https://doi.org/10.1017/S0016756815000515

Lebedev, S., Schaeffer, A. J., Fullea, J., & Pease, V. (2017). Seismic tomography of the Arctic region: inferences for the thermal structure and evolution of the lithosphere. *Geological Society, London, Special Publications*, 460, 419–440. https://doi.org/10.1144/SP460.10

Lei, J., & Zhao, D. (2005). P-wave tomography and origin of the Changbai intraplate volcano in Northeast Asia. Tectonophysics, 397(3–4), 281–295. https://doi.org/10.1016/j.tecto.2004.12.009

Levshin, A. L., Shen, W., Barmin, M. P., & Ritzwoller, M. H. (2017). Surface wave studies of the Greenland upper lithosphere using ambient seismic noise. https://pdfs.semanticscholar.org/977c/ce2101b7f9b384d38e9b051bf289a7277b54.pdf

Lu, C., Grand, S. P., Lai, H., & Garnero, E. J. (2019). TX2019slab: A new P and S tomography model incorporating subducting slabs. Journal of Geophysical Research: Solid Earth, 124, 11549–11567. https://doi.org/10.1029/2019JB017448

Martos, Y. M., Jordan, T. A., Catalán, M., Jordan, T. M., Bamber, J. L., & Vaughan, D. G. (2018). Geothermal heat flux reveals the Iceland hotspot track underneath Greenland. *Geophysical Research Letters*, 45, 8214–8222. https://doi.org/10.1029/2018GL078289

Mordret, A. (2018). Uncovering the Iceland hot spot track beneath Greenland. *Journal of Geophysical Research: Solid Earth*, 123, 4922–4941. https://doi.org/10.1029/2017JB015104

Mordret, A., Mikesell, T. D., Harig, C., Lipovsky, B. P., & Prieto, G. A. (2016). Monitoring southwest Greenland's ice sheet melt with ambient seismic noise. *Science Advances*, 2(5), e1501538. http://dx.doi.org/10.1126/sciadv.1501538

Müller, R. D., Cannon, J., Qin, X., Watson, R. J., Gurnis, M., Williams, S., et al. (2018). GPlates: Building a virtual Earth through deep time. *Geochemistry, Geophysics, Geosystems*, 19, 2243–2261. https://doi.org/10.1029/2018GC007584

Müller, R. D., Zahirovic, S., Williams, S. E., Cannon, J., Seton, M., Bower, D. J., Tetley, M. G., Heine, C., Le Breton, E., Liu, S., Russell, S. H. J., Yang, T., Leonard, J., & Gurnis, M. (2019). A global plate model including lithospheric deformation along major rifts and orogens since the Triassic. *Tectonics*, 38(6), 1884-1907. https://doi.org/10.1029/2018TC005462

Nakakuki, T., Tagawa, M., & Iwase, Y. (2010). Dynamical mechanisms controlling formation and avalanche of a stagnant slab. *Physics of the Earth and Planetary Interiors*, 183, 309–320. https://doi.org/10.1016/j.pepi.2010.02.003

Navarrete, C., Gianni, G., Massaferro, G., & Butler, K. (2020). The fate of the Farallon slab beneath Patagonia and its links to Cenozoic intraplate magmatism, marine transgressions and topographic uplift. Earth-Science Reviews, 210, 103379. https://doi.org/10.1016/j.earscirev.2020.103379

Paige, C. C., & Saunders, M. A. (1982). LSQR, An algorithm for sparse linear equations and sparse least squares. *ACM Transactions on Mathematical Software (TOMS)*, 8(1), 43–71. https://doi.org/10.1145/355984.355989

Peace, A. L., Foulger, G. R., Schiffer, C., & McCaffrey, K. J. (2017). Evolution of Labrador Sea–Baffin Bay: Plate or plume processes? *Geoscience Canada*, 44(3), 91–102. https://doi.org/10.12789/geocanj.2017.44.120

Peng, D., & Liu, L. (2021). A newly discovered Late-Cretaceous East Asian flat slab explains its unique lithospheric structure and tectonics. https://doi.org/10.1002/essoar.10506583.1

Pilidou, S., Priestley, K., Gudmundsson, Ó., & Debayle, E. (2004). Upper mantle S‐wave speed heterogeneity and anisotropy beneath the North Atlantic from regional surface wave tomography: The Iceland and Azores plumes. *Geophysical Journal International*, 159, 1057–1076. https://doi.org/10.1111/j.1365‐246X.2004.02462.x

Pourpoint, M., Anandakrishnan, S., Ammon, C. J., & Alley, R. B. (2018). Lithospheric structure of Greenland from ambient noise and earthquake surface wave tomography. *Journal of*

Geophysical Research: Solid Earth, 123, 7850–7876. https://doi.org/10.1029/2018JB015490

Rickers, F., Fichtner, A., & Trampert, J. (2013). The Iceland–Jan Mayen plume system and its impact on mantle dynamics in the North Atlantic region: Evidence from full-waveform inversion. *Earth and Planetary Science Letters*, 367, 39–51. https://doi.org/10.1016/j.epsl.2013.02.022

Ritsema, J., Deuss, A., van Heijst, H. J., & Woodhouse, J. H. (2011). S40RTS: a degree-40 shear-velocity model for the mantle from new Rayleigh wave dispersion, teleseismic traveltime and normal-mode splitting function measurements. Geophysical Journal International, 184, 1223–1236. https://doi.org/10.1111/j.1365-246X.2010.04884.x

Schmid, C., Goes, S., van der Lee, S., & Giardini, D. (2002). Fate of the Cenozoic Farallon slab from a comparison of kinematic thermal modeling with tomographic images. *Earth and Planetary Science Letters*, 204(1–2), 17–32. https://doi.org/10.1016/S0012-821X(02)00985-8

Simmons, N. A., Forte, A. M., Boschi, V., & Grand, S. P. (2010). GyPSuM: A joint tomographic model of mantle density and seismic wave speeds. Journal of Geophysical Research: Solid Earth, 115(B12), B12310. https://doi.org/10.1029/2010JB007631

Simmons, N. A., Myers, S. C., Johannesson, G., & Matzel, E. (2012). LLNL-G3Dv3: Global P wave tomography model for improved regional and teleseismic travel time prediction. Journal of Geophysical Research: Solid Earth, 117, B10302. https://doi.org/10.1029/2012JB009525

Takenaka, H., Komatsu, M., Toyokuni, G., Nakamura, T., & Okamoto, T. (2017). Quasi-Cartesian finite-difference computation of seismic wave propagation for a three-dimensional sub-global model. *Earth, Planets and Space*, 69, 67. https://doi.org/10.1186/s40623-017-0651-1

Toyokuni, G., & Zhao, D. (2021). P wave tomography for 3-D radial and azimuthal anisotropy beneath Greenland and surrounding regions. https://doi.org/10.1002/essoar.10506588.1

Toyokuni, G., Kanao, M., Tono, Y., Himeno, T., Tsuboi, S., Childs, D., Anderson, K., & Takenaka, H. (2014). Monitoring of the Greenland ice sheet using a broadband seismometer network: the GLISN project. *Antarctic Record*, 58(1), 1–18. http://doi.org/10.15094/00009722

Toyokuni, G., Komatsu, M., & Takenaka, H. (2021a). Estimation of seismic attenuation of the Greenland Ice Sheet using 3-D waveform modeling. *Journal of Geophysical Research: Solid Earth*. https://doi.org/10.1029/2021JB021694

Toyokuni, G., Matsuno, T., & Zhao, D. (2020a). *P* wave tomography beneath Greenland and surrounding regions: 1. Crust and upper mantle. *Journal of Geophysical Research: Solid Earth*, 125, e2020JB019837. https://doi.org/10.1029/2020JB019837

Toyokuni, G., Matsuno, T., & Zhao, D. (2020b). *P* wave tomography beneath Greenland and surrounding regions: 2. Lower mantle. *Journal of Geophysical Research: Solid Earth*, 125, e2020JB019839. https://doi.org/10.1029/2020JB0198379

Toyokuni, G., Takenaka, H., Kanao, M., Tsuboi, S., & Tono, Y. (2015). Numerical modeling of seismic waves for estimating the influence of the Greenland ice sheet on observed seismograms. *Polar Science*, 9(1), 80–93. https://doi.org/10.1016/j.polar.2014.12.001

Toyokuni, G., Takenaka, H., Takagi, R., Kanao, M., Tsuboi, S., Tono, Y., Childs, D., & Zhao, D. (2018). Changes in Greenland ice bed conditions inferred from seismology. *Physics of the Earth and Planetary Interiors*, 277, 81–98. https://doi.org/10.1016/j.pepi.2017.10.010

Toyokuni, G., Zhao, D., & Chen, K. H. (2021b). Structural control on the 2018 and 2019 Hualien earthquakes in Taiwan. *Physics of the Earth and Planetary Interiors*, 312, 106673. https://doi.org/10.1016/j.pepi.2021.106673

Um, J., & Thurber, C. (1987). A fast algorithm for two-point seismic ray tracing. *Bulletin of the Seismological Society of America*, 77(3), 972–986.

Wessel, P., Smith, W. H. F., Scharroo, R., Luis, J., & Wobbe, F. (2013). Generic Mapping Tools: Improved Version Released. *Eos, Transactions, American Geophysical Union*, 94(45), 409. https://doi.org/10.1002/2013EO450001

Zhao, D. (2004). Global tomographic images of mantle plumes and subducting slabs: Insight into deep Earth dynamics. *Physics of the Earth and Planetary Interiors*, 146(1–2), 3–34. https://doi.org/10.1016/j.pepi.2003.07.032

Zhao, D., Fujisawa, M., & Toyokuni, G. (2017). Tomography of the subducting Pacific slab and the 2015 Bonin deepest earthquake (Mw 7.9). *Scientific Reports*, 7, 44487. https://doi.org/10.1038/srep44487

Zhao, D., Tian, Y., Lei, J., Liu, L., & Zheng, S. (2009). Seismic image and origin of the Changbai intraplate volcano in East Asia: Role of big mantle wedge above the stagnant Pacific slab. *Physics of the Earth and Planetary Interiors*, 173(3–4), 197–206. https://doi.org/10.1016/j.pepi.2008.11.009

Zhao, D., Toyokuni, G., & Kurata, K. (2021). Deep mantle structure and origin of Cenozoic intraplate volcanoes in Indochina, Hainan and South China Sea. *Geophysical Journal International*, 225(1), 572–588. https://doi.org/10.1093/gji/ggaa605

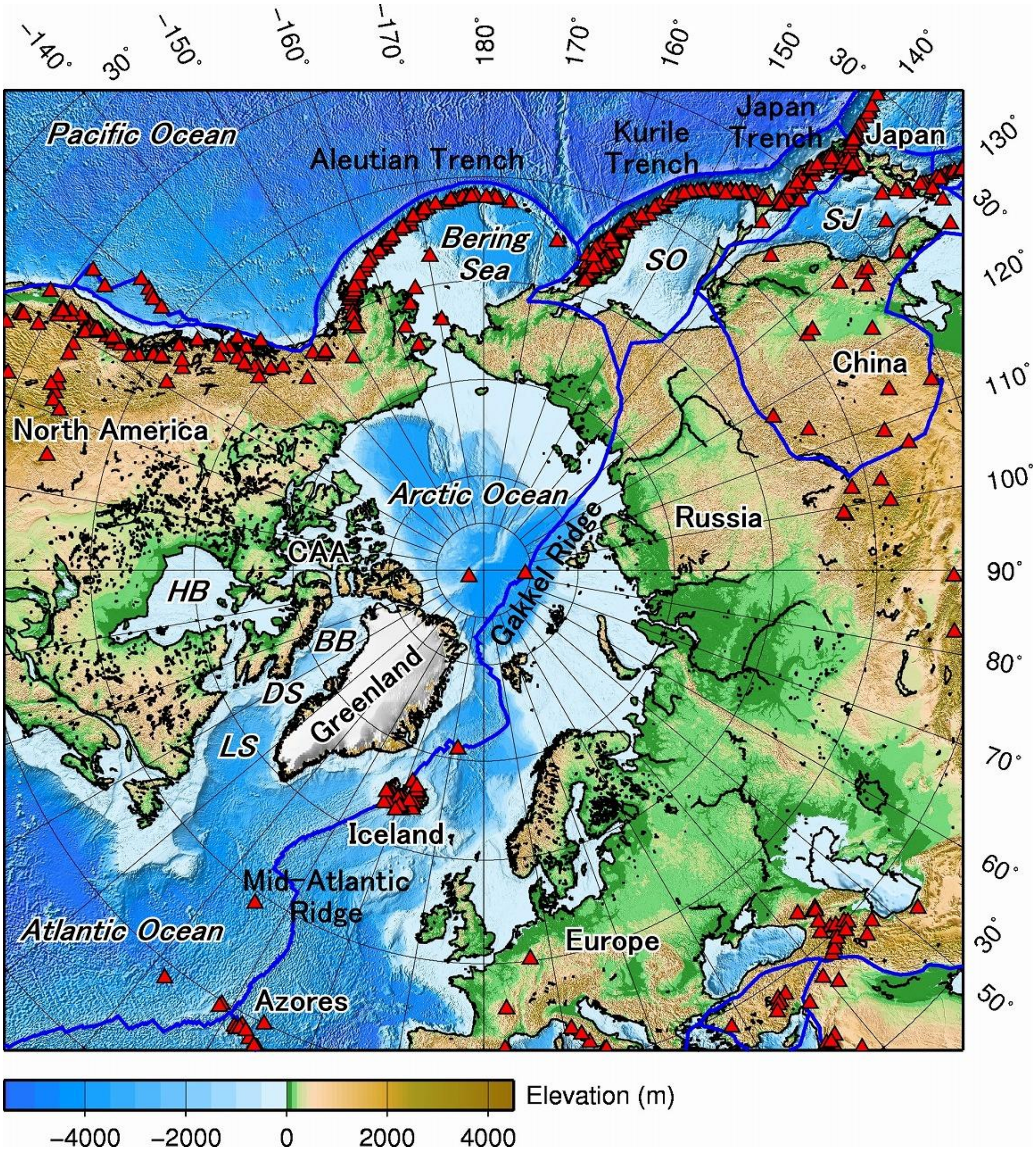
Pacific Ocean
Aleutian Trench
Kurile Trench
Japan Trench
Japan
Bering Sea
SO
SJ
China
North America
Arctic Ocean
Gakkel Ridge
Russia
CAA
HB
BB
DS
Greenland
LS
Iceland
Mid-Atlantic Ridge
Atlantic Ocean
Europe
Azores
Elevation (m)
−4000
−2000
0
2000
4000

440

Figure 1. Map of the circum-Arctic region. The color scale for the topography is shown at the bottom. White color denotes the Greenland Ice Sheet. Red triangles: active volcanoes; thick blue lines: plate boundaries. CAA = Canadian Arctic Archipelago; BB = Baffin Bay; DS = Davis Strait; HB = Hudson Bay; LS = Labrador Sea; SJ = Sea of Japan; SO = Sea of Okhotsk.

446 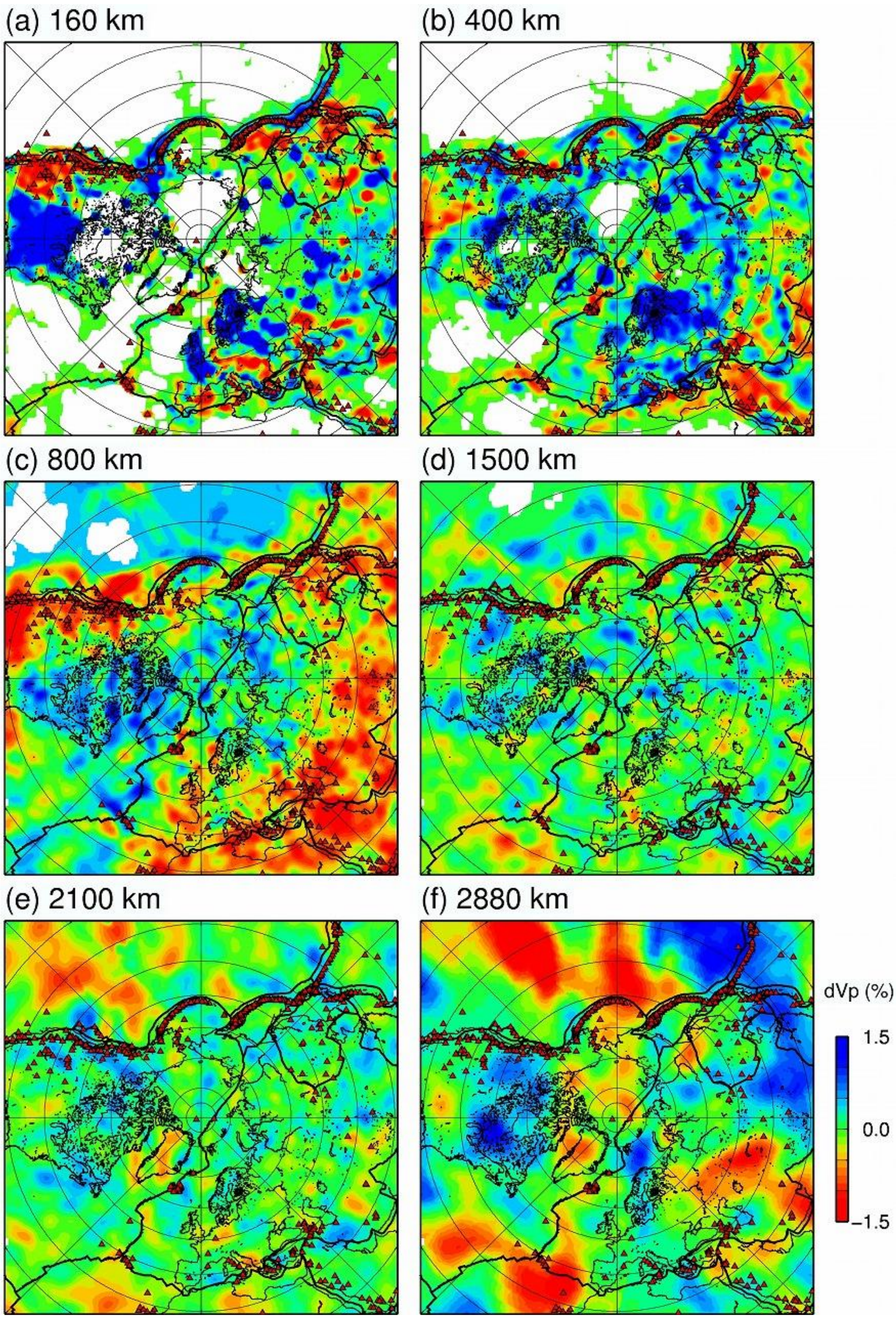

Figure 2. Map views of Vp tomography at six depths obtained by this study. The layer depth is shown above each map. The blue and red colors denote high and low Vp perturbations, respectively, whose scale (in %) is shown on the right. Areas with average hit counts < 20 are masked in white. Red triangles: active volcanoes; thick black lines: plate boundaries.

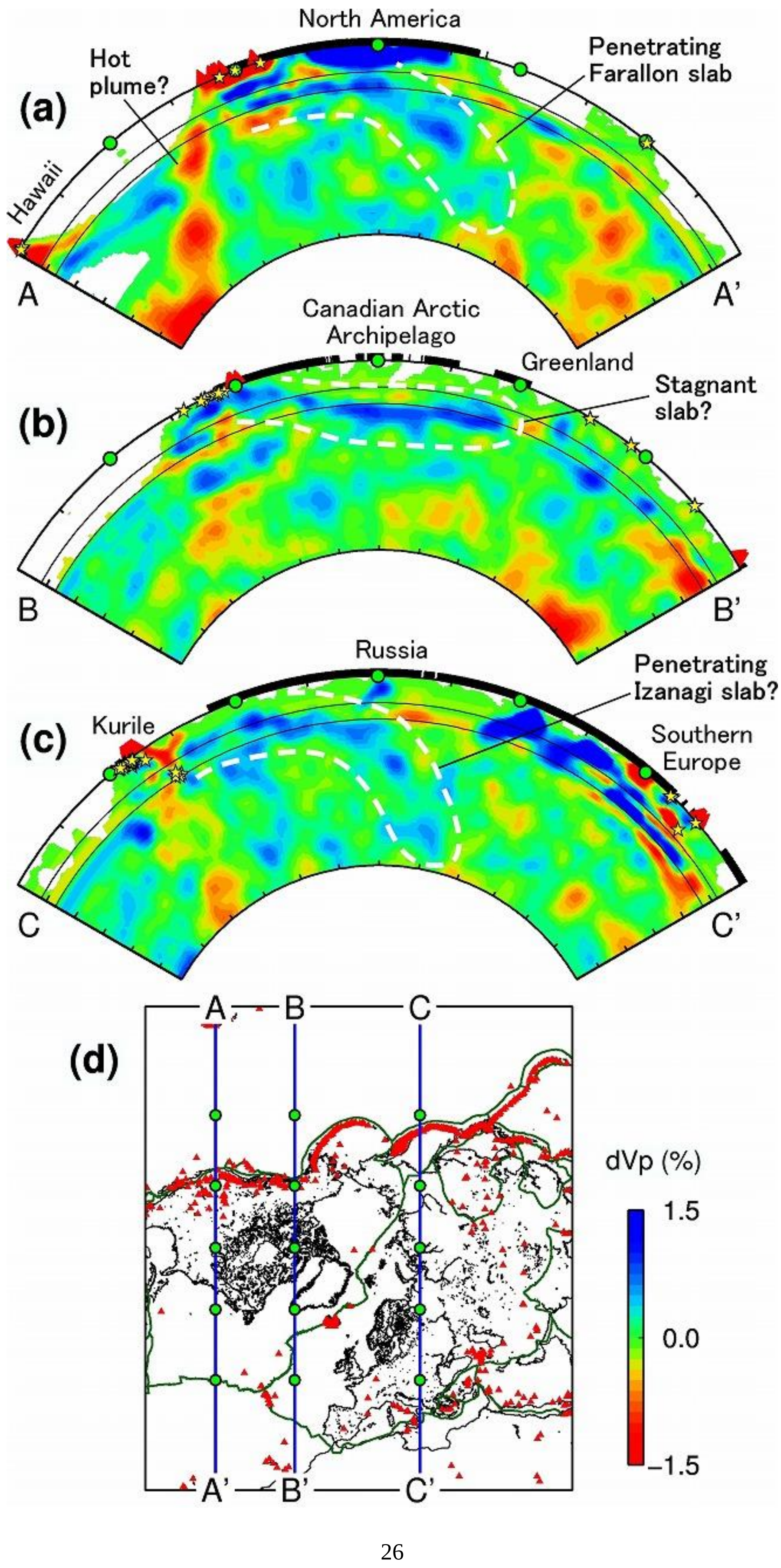

North America
Hot plume?
Penetrating Farallon slab
(a)
Hawaii
A
A'
Canadian Arctic Archipelago
Greenland
Stagnant slab?
(b)
B
B'
Russia
Penetrating Izanagi slab?
Kurile
Southern Europe
(c)
C
C'
(d)
A
B
C
A'
B'
C'
dVp (%)
1.5
0.0
–1.5

451

Figure 3. Vertical cross sections of Vp tomography showing main tectonic features. **(a–c)** Vertical cross sections along three profiles as shown on the map **(d)**. The scale for Vp perturbation (in %) is shown on the right. The 410 and 660 km discontinuities are shown in black solid lines. The thick black lines on the surface denote land areas. Areas with average hit counts < 20 are masked in white. Red triangles: active volcanoes existing within ±2° of each profile; yellow stars: large earthquakes ($M \geq 6$) that occurred during 1964–2015 within ±2° of each profile; green circles: points dividing the section equidistantly using the central angle of the earth, which correspond to those in **(d)**. In the map **(d)**, red triangles: active volcanoes; thick green lines: plate boundaries.

461 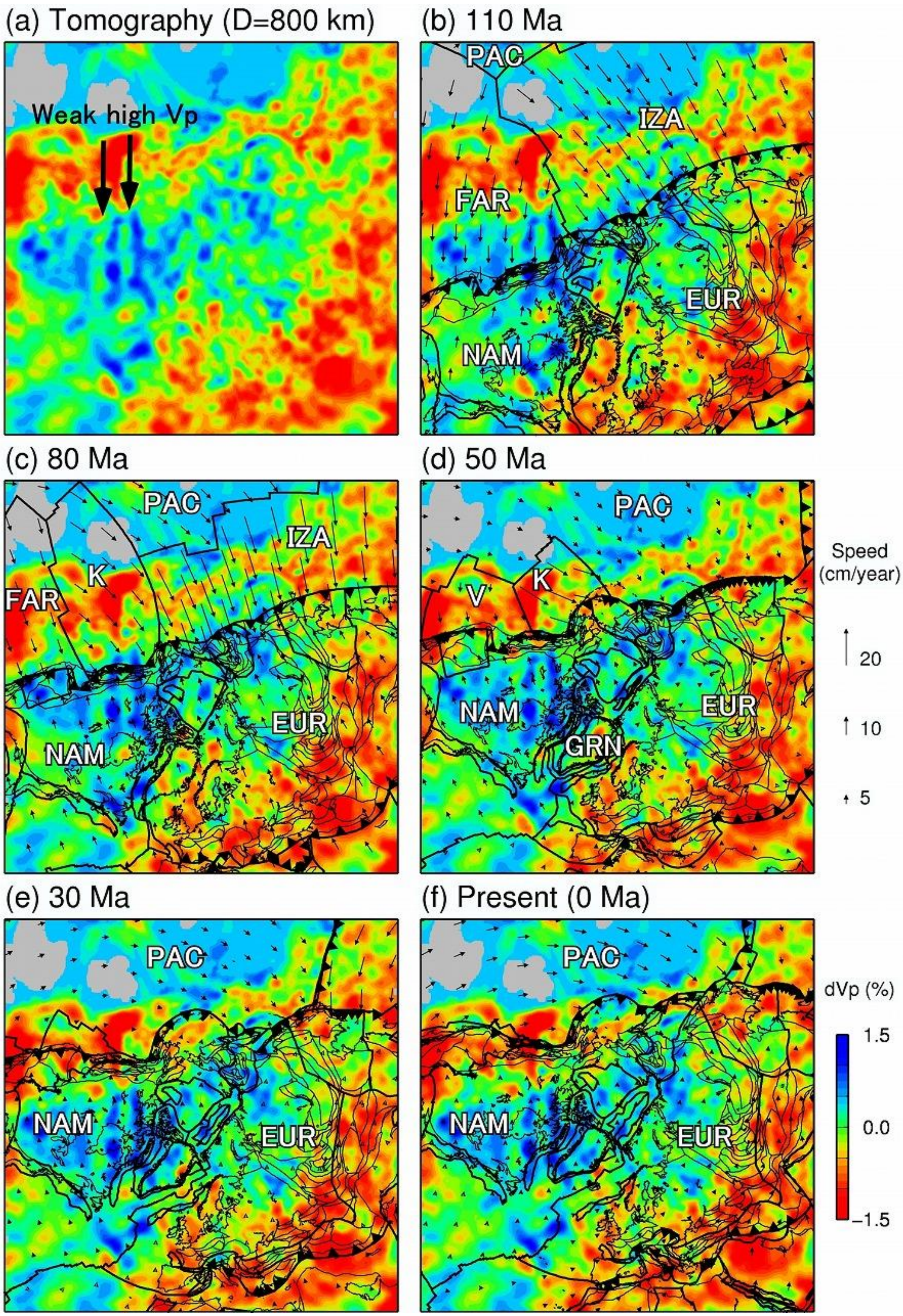
(a) Tomography (D=800 km)
Weak high Vp
(b) 110 Ma
PAC
IZA
FAR
EUR
NAM
(c) 80 Ma
PAC
IZA
K
FAR
EUR
NAM
(d) 50 Ma
PAC
V
K
NAM
EUR
GRN
Speed (cm/year)
20
10
5
(e) 30 Ma
PAC
NAM
EUR
(f) Present (0 Ma)
PAC
NAM
EUR
dVp (%)
1.5
0.0
−1.5

Figure 4. **(a)** Map views of Vp tomography at a depth of 800 km (same as in Figure 2c) and **(b–f)** comparison with plate reconstructions (Müller et al., 2019) from 110 Ma to the present day. The scale for Vp perturbation (in %) is shown on the right. In **(a)**, thick arrows show locations of weak high Vp lineaments. In **(b–f)**, the age of reconstruction is shown above each panel. Black toothed lines delineate subduction zones, and other black lines denote mid-ocean ridges and transform faults. The length and azimuth of each arrow denote the speed and direction of the absolute plate motion, respectively. The scale for plate speed is shown on the right. EUR = Eurasian Plate; FAR = Farallon Plate; GRN = Greenland Plate; IZA = Izanagi Plate; K = Kula Plate; NAM = North American Plate; PAC = Pacific Plate; V = Vancouver Plate.

473 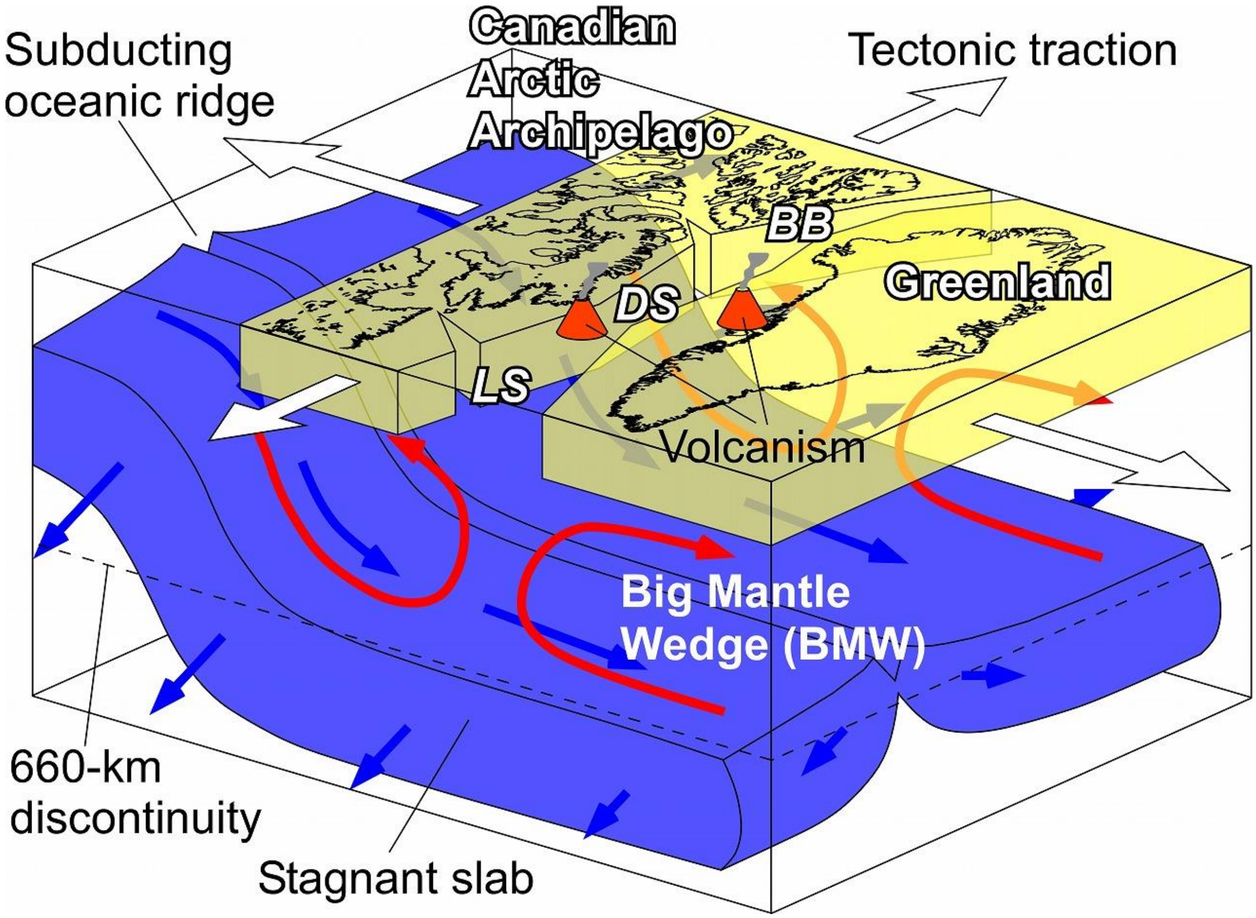

474 **Figure 5**. Schematic diagram showing a possible mechanism of the division between Greenland
475 and Canada and tearing of crust beneath the Canadian Arctic Archipelago revealed by this study.
476 The subducting slab with oceanic ridge becomes stagnant beneath the 660-km discontinuity
477 beneath Canada and Greenland. The red arrows indicate upwelling of hot asthenospheric
478 materials due to convective circulation process in the Big Mantle Wedge. The blue arrows
479 indicate subduction and divergence directions of the subducted slab. The white arrows on the
480 surface indicate tectonic traction, whose length conceptually indicates the traction strength. BB =
481 Baffin Bay; DS = Davis Strait; LS = Labrador Sea.

Geophysical Research Letters

Supporting Information for

Arctic rift system driven by a giant stagnant slab

Genti Toyokuni[1] and Dapeng Zhao[1]

1 Department of Geophysics, Graduate School of Science, Tohoku University, Sendai 980-8578, Japan

Contents of this file

- Figures S1 to S29
- Tables S1 and S2

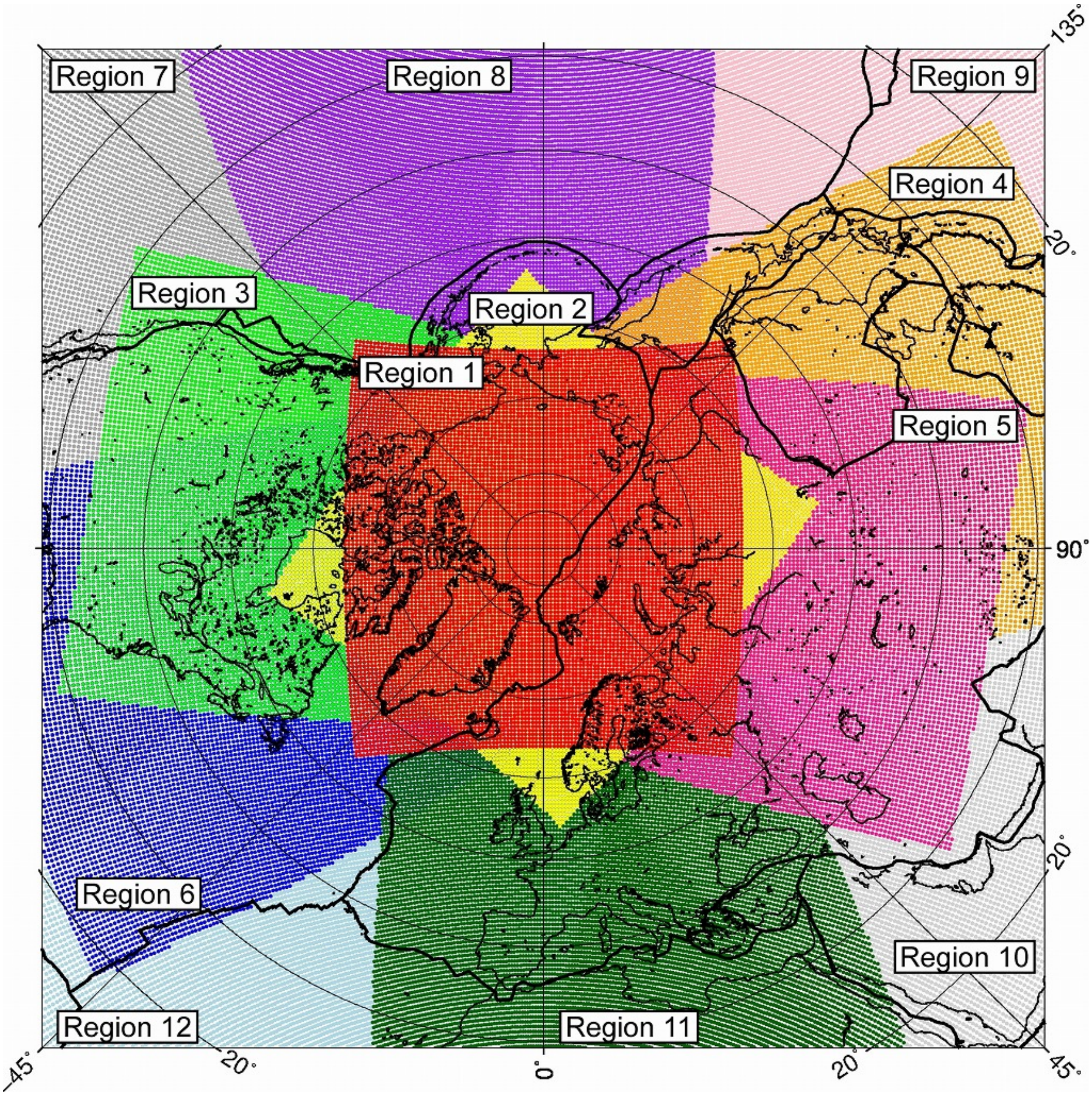

Figure S1. Distribution of Regions 1−12 listed in Table S1. The points denote the grid nodes adopted for interpolation to obtain the final tomographic model.

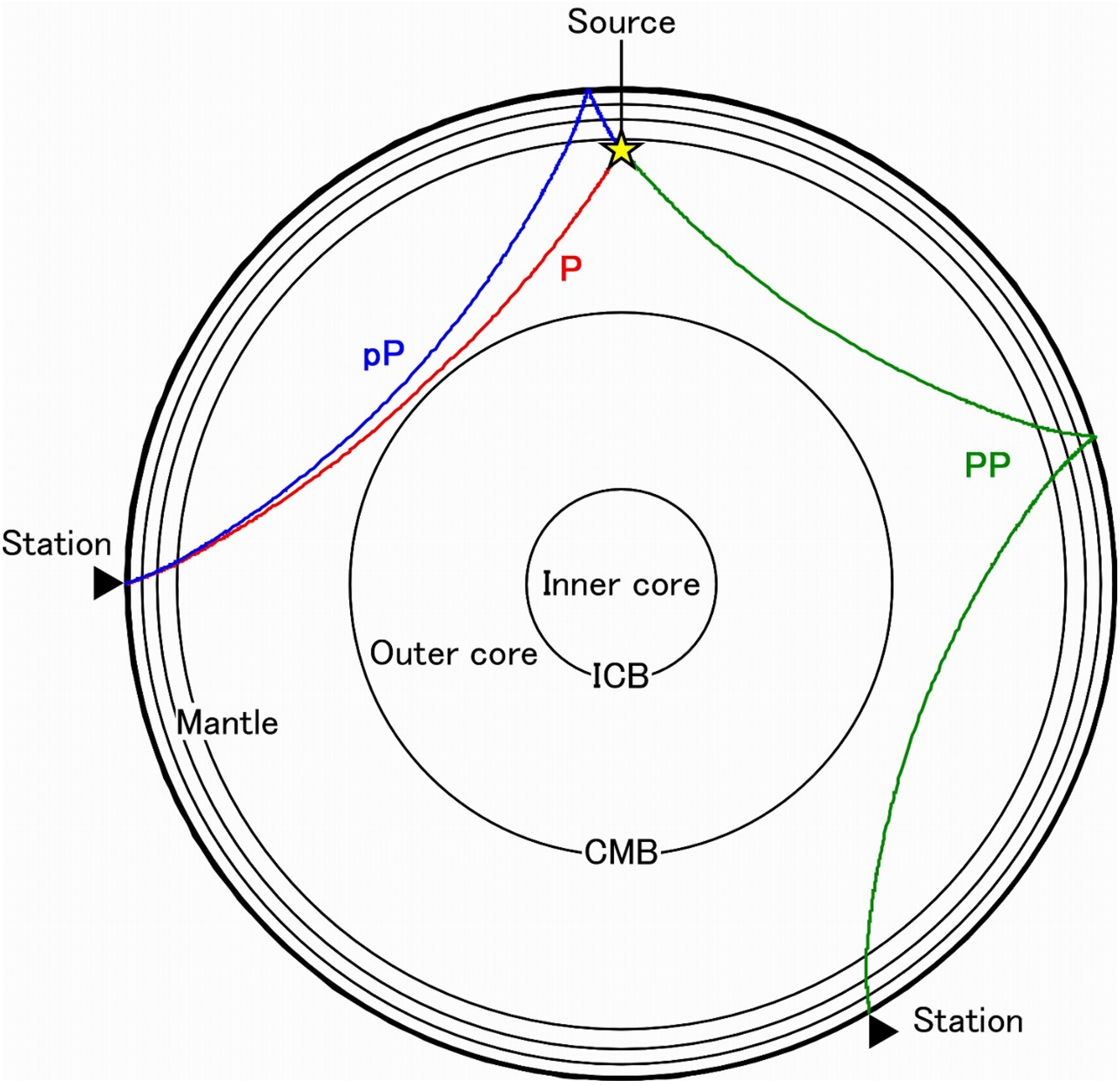

Figure S2. Schematic illustration of ray paths of *P*, *pP*, and *PP* waves. The yellow star denotes a hypocenter. The inverted triangles denote seismic stations.

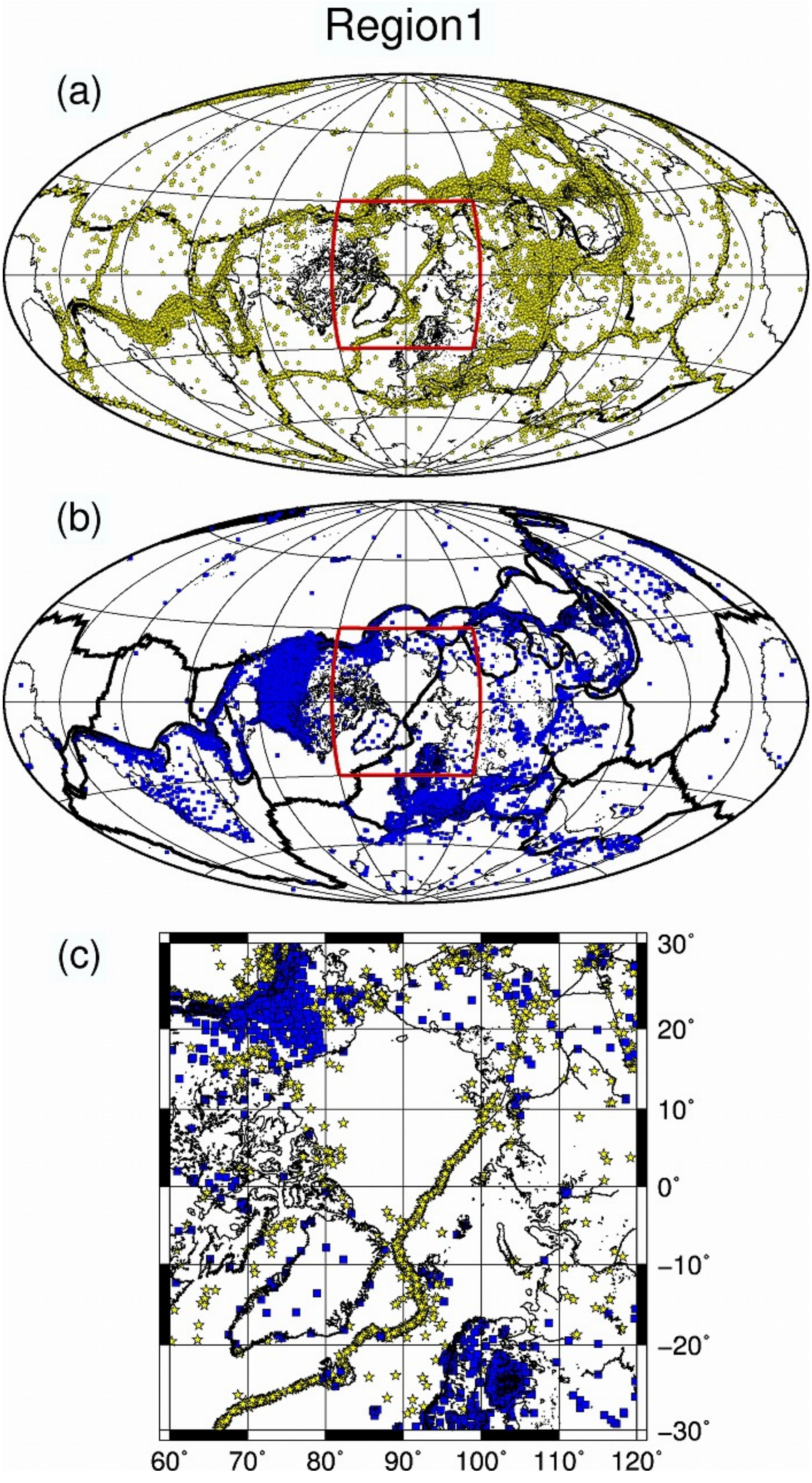

Figure S3.

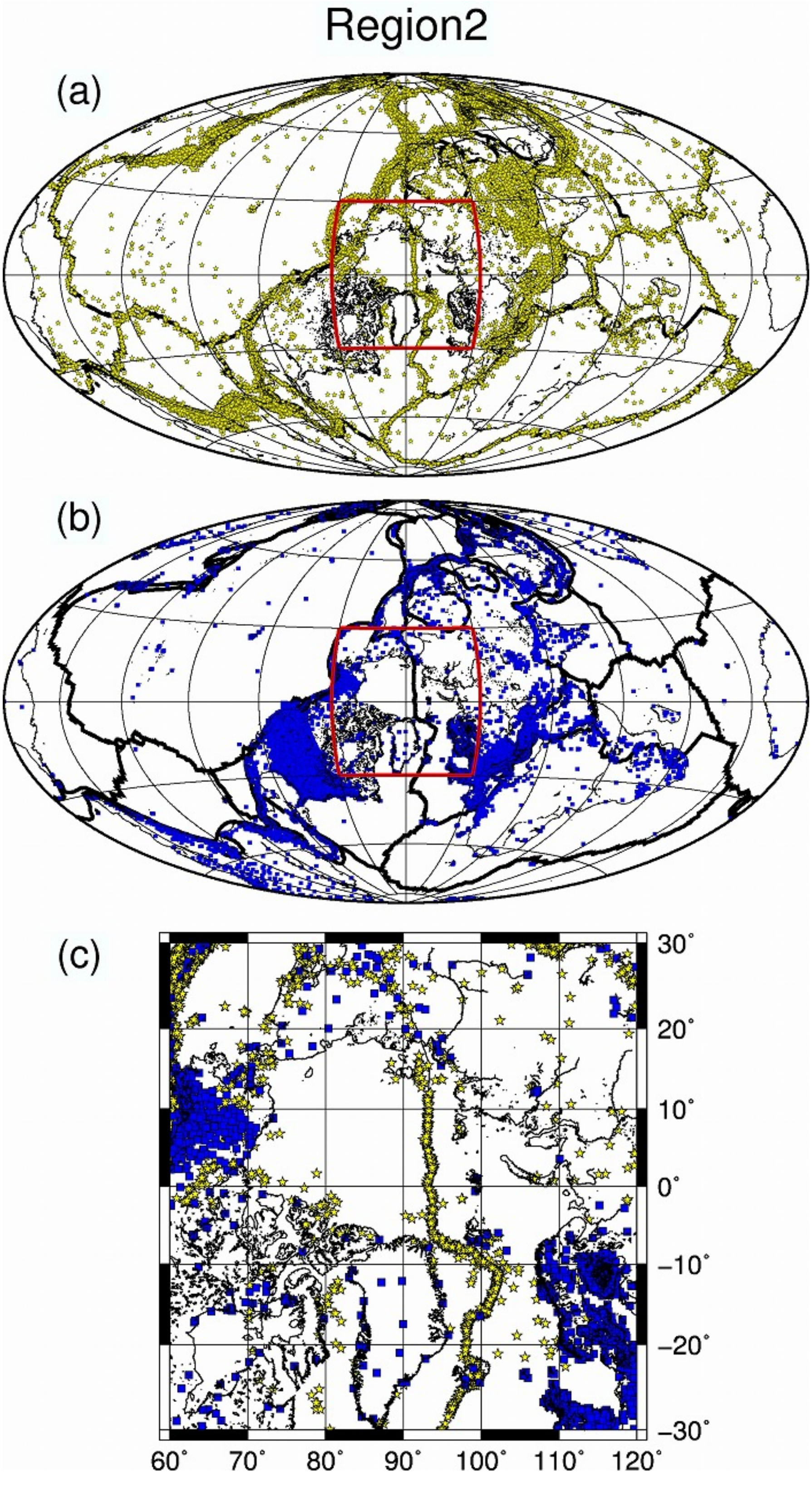

Figure S4.

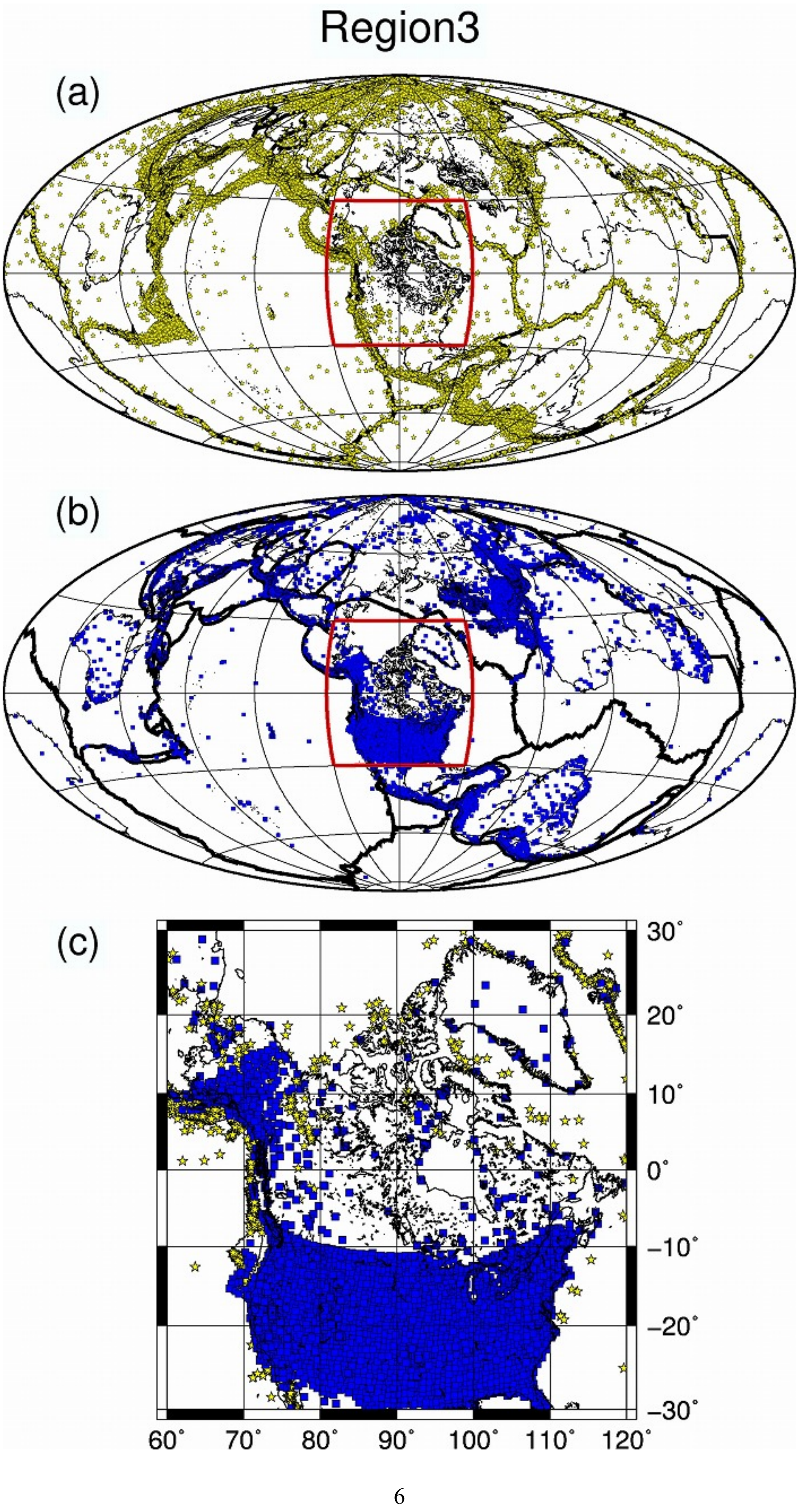

Figure S5.

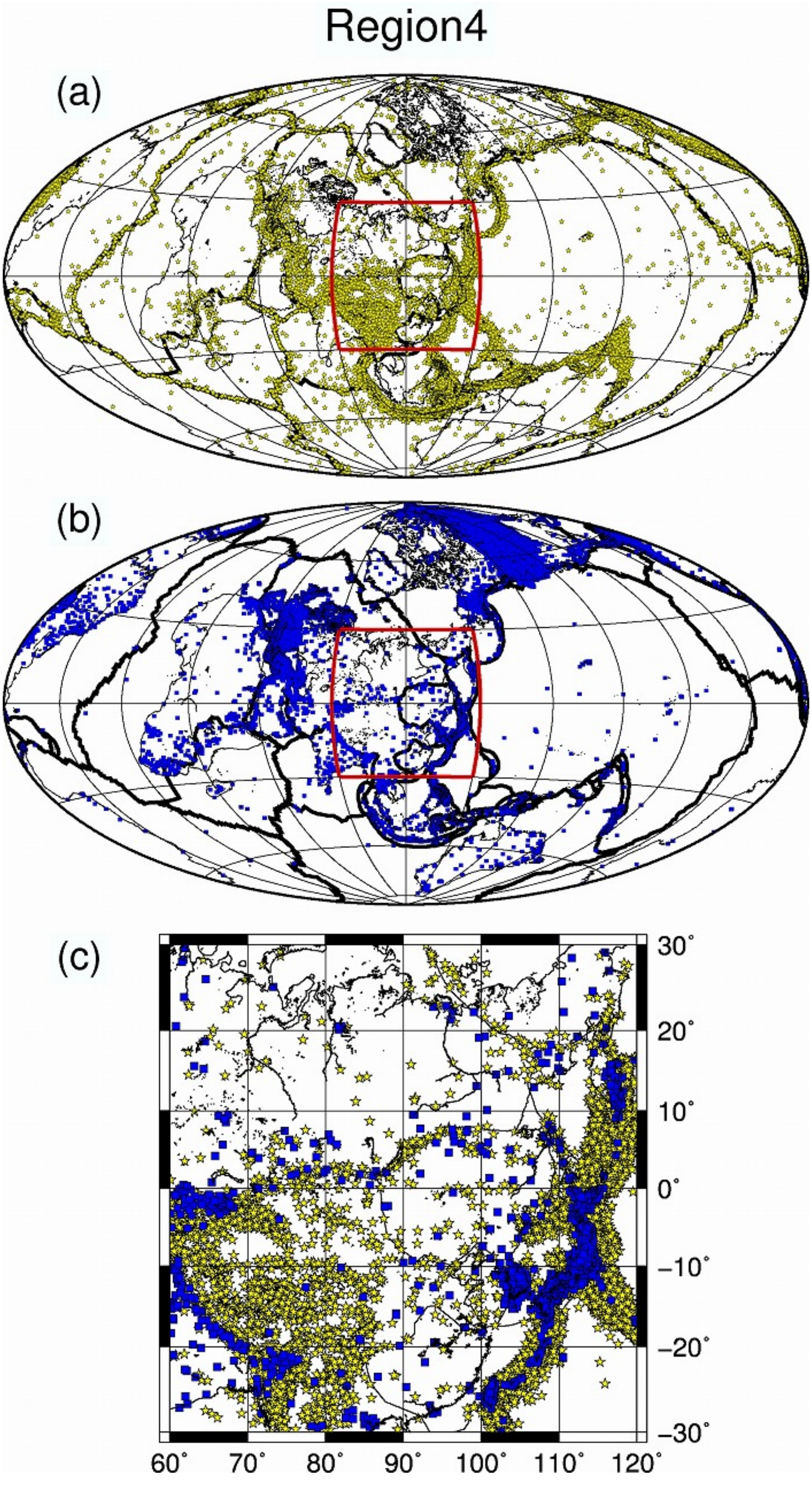

Figure S6.

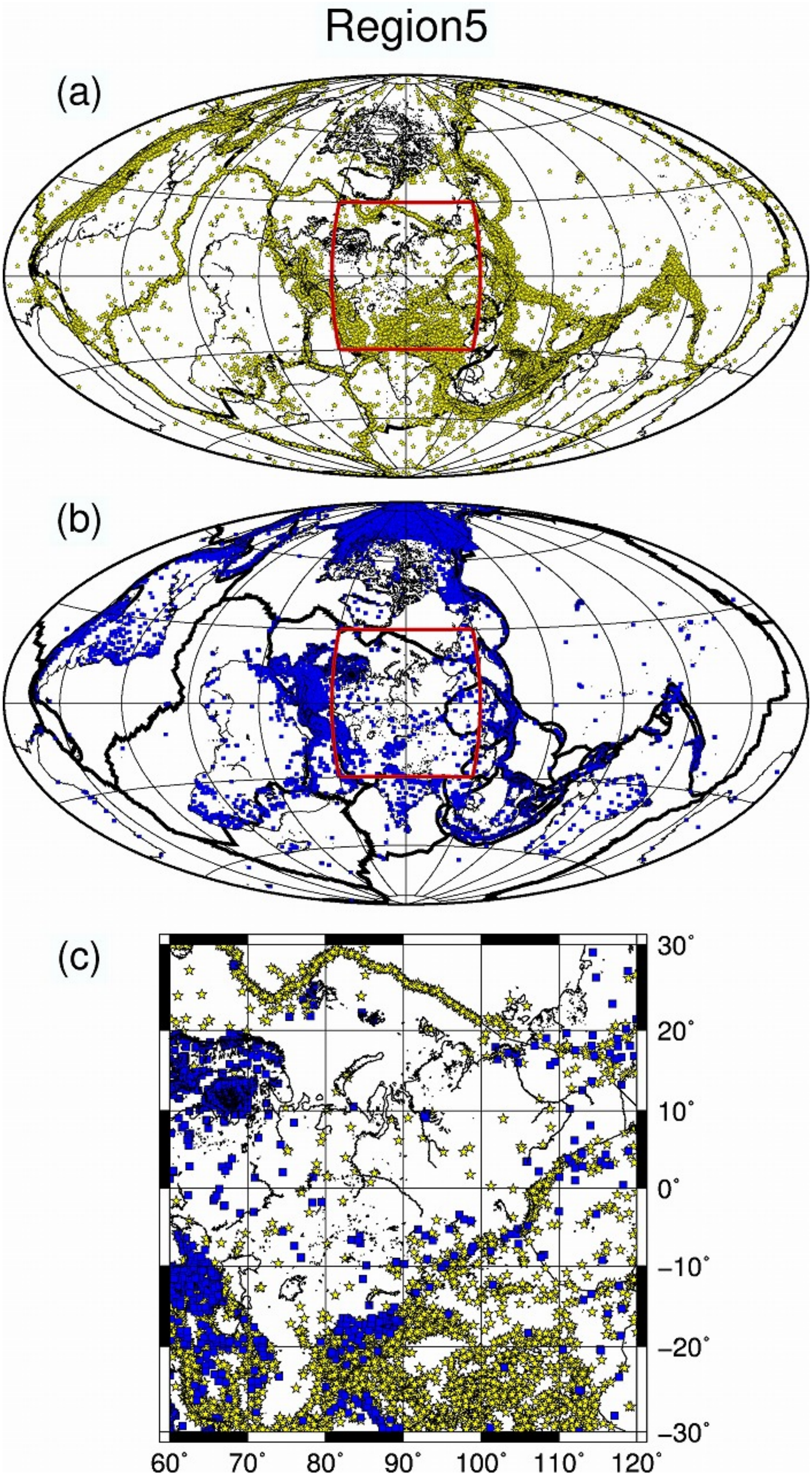

Figure S7.

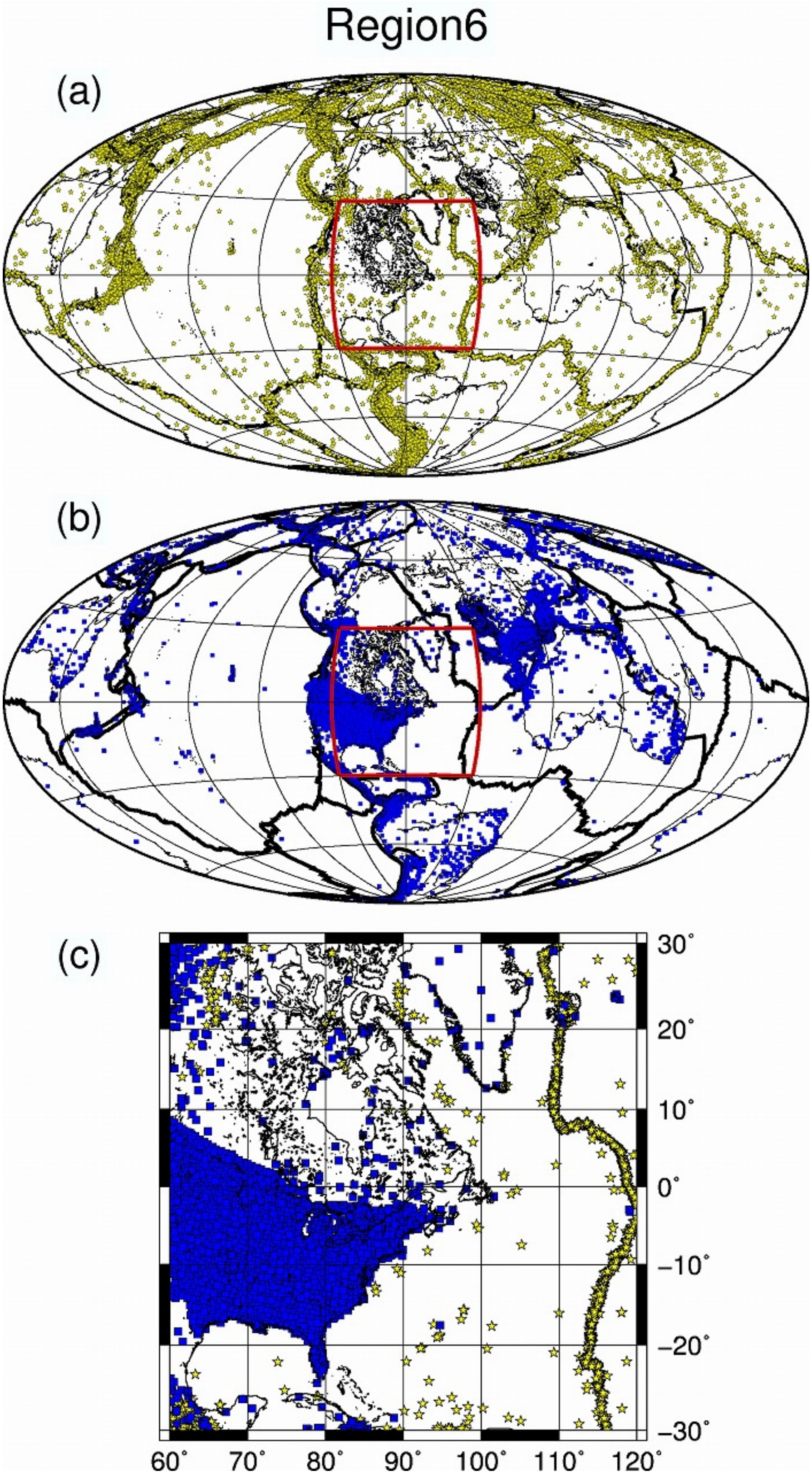

Figure S8.

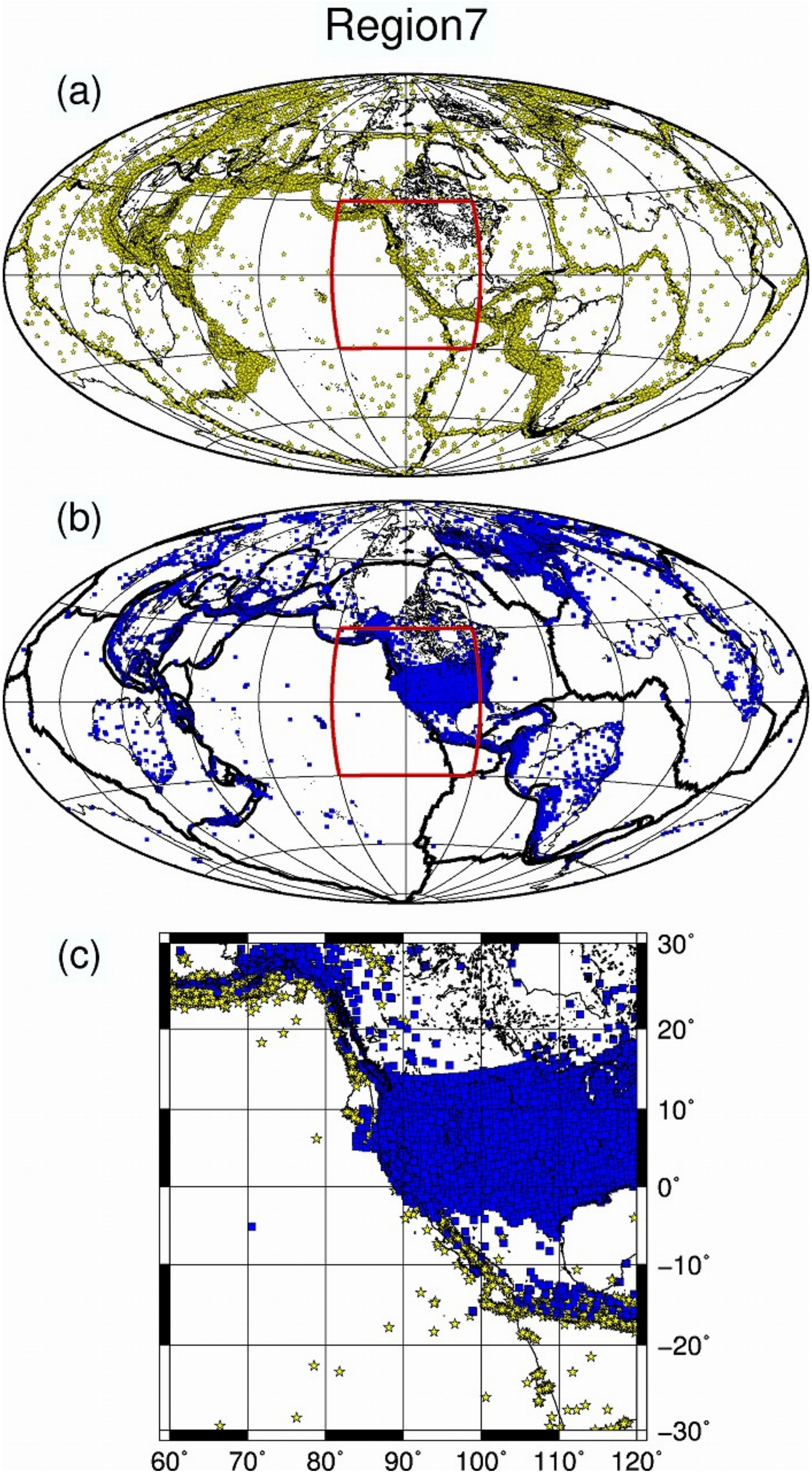

Figure S9.

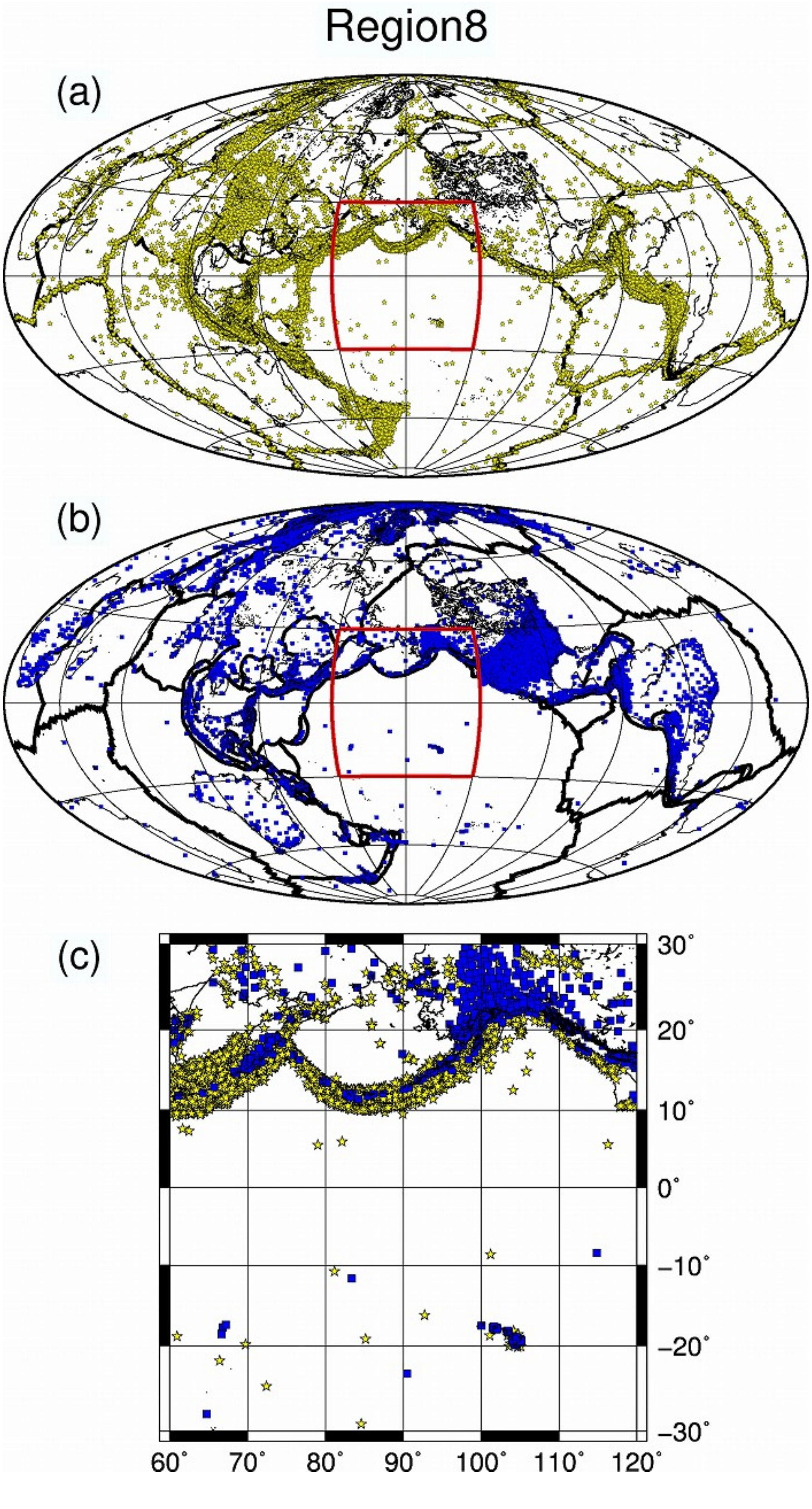

Figure S10.

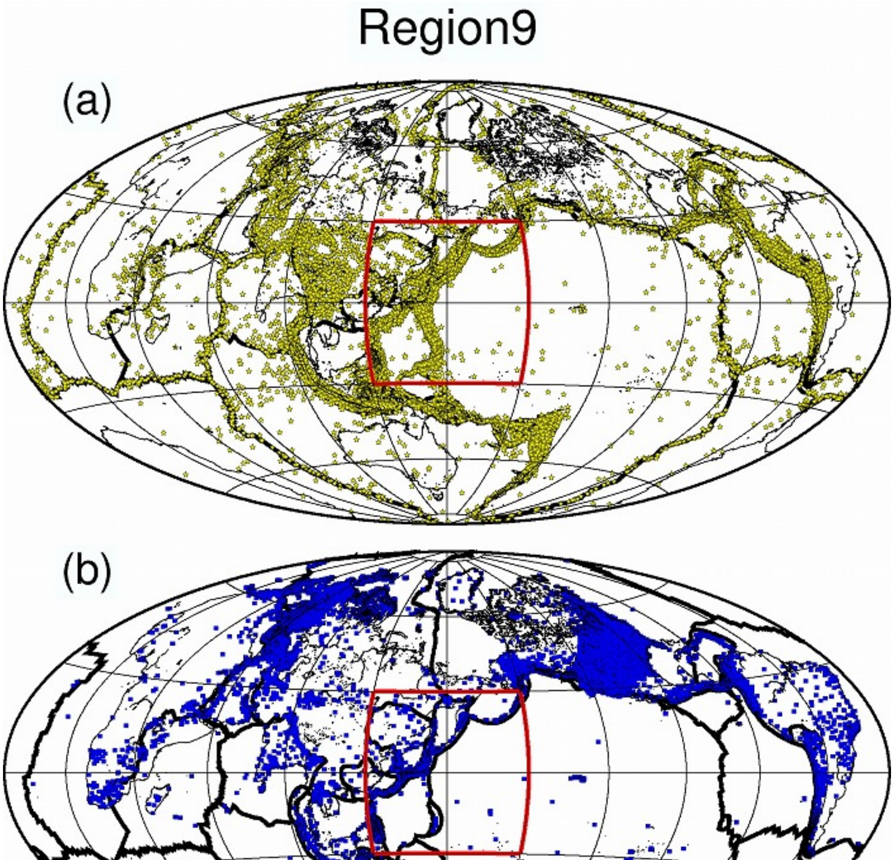

Figure S11.

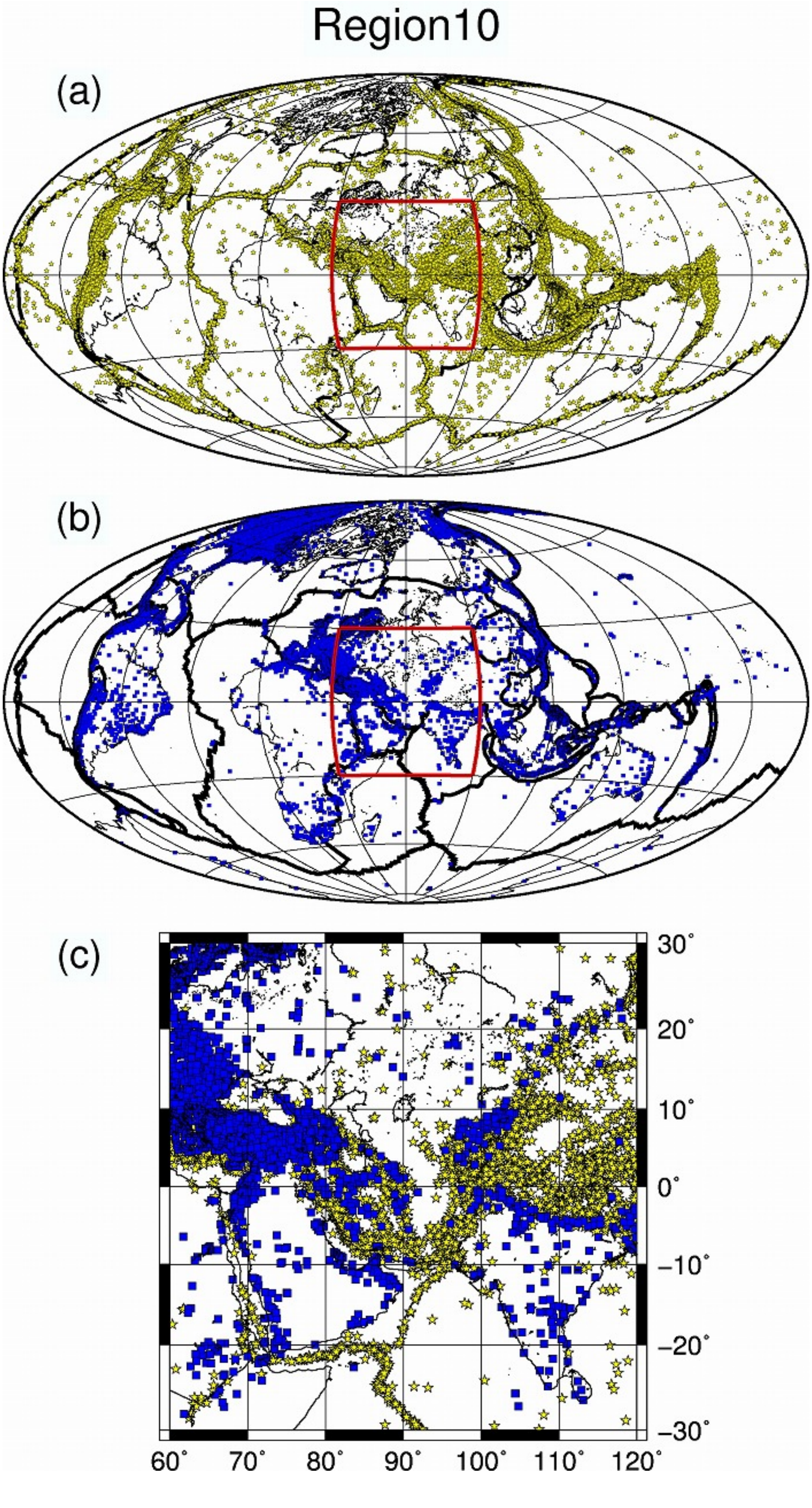

Figure S12.

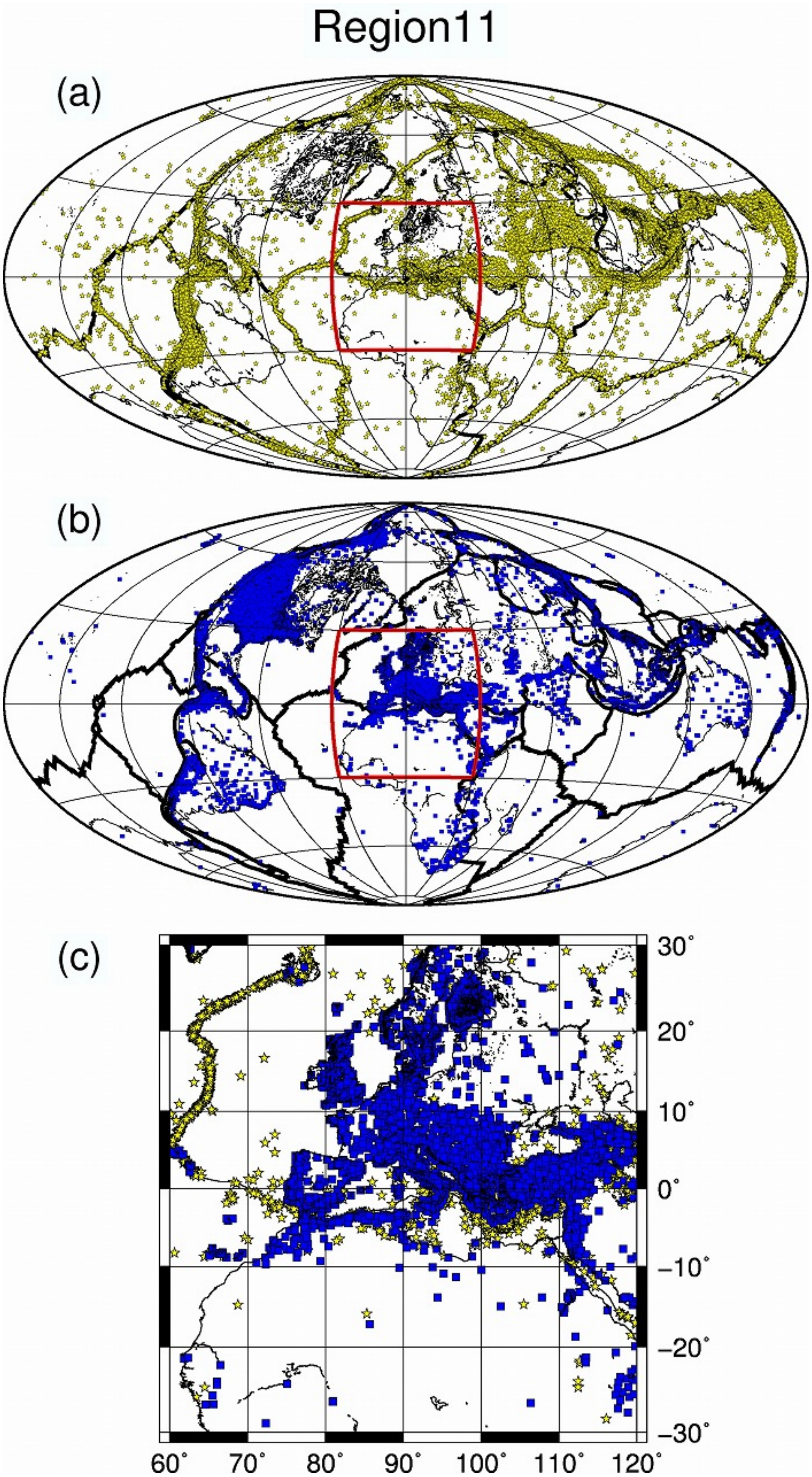

Figure S13.

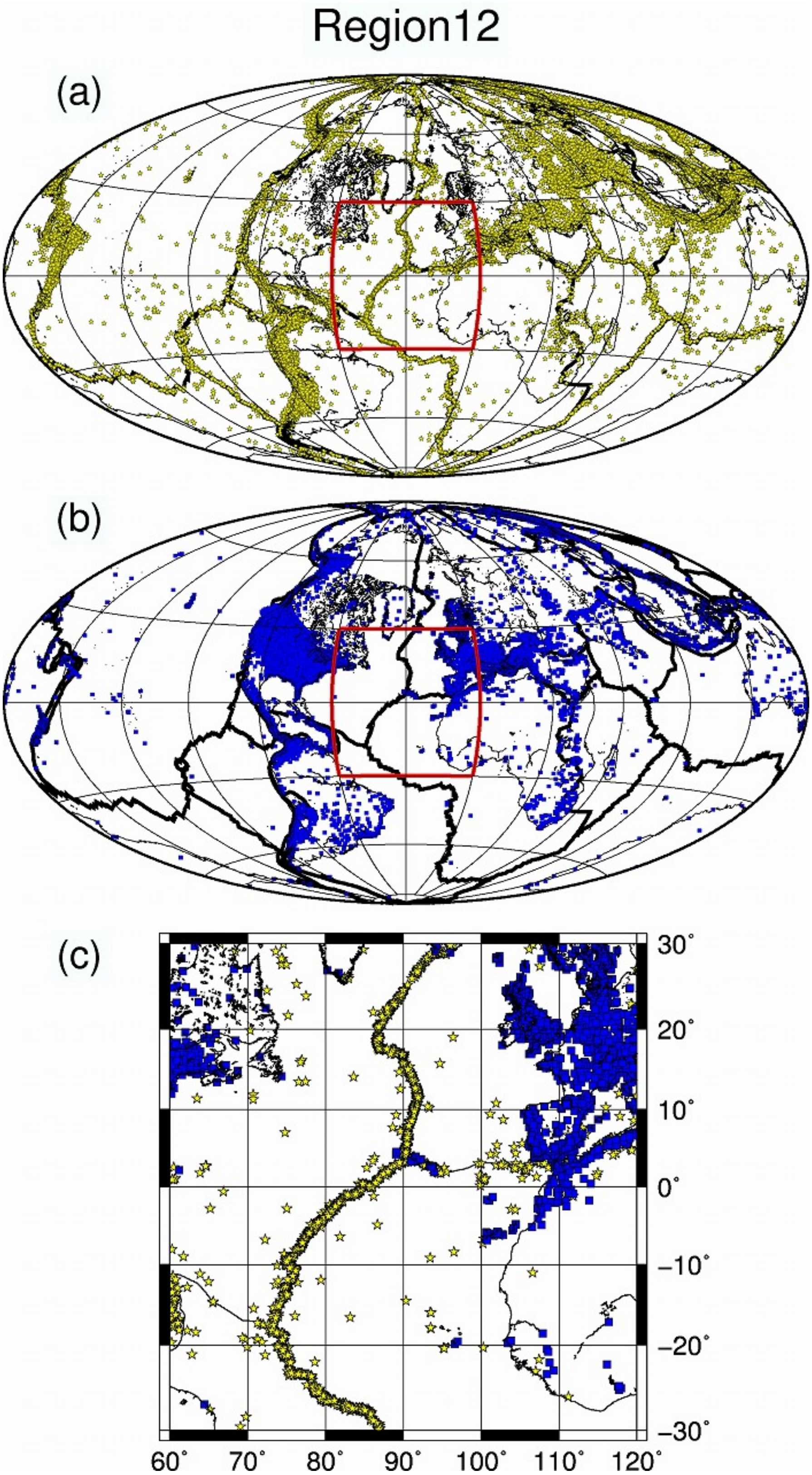

Figure S14.

Figure 3. Global distribution of **(a)** earthquakes and **(b)** seismic stations, and **(c)** distribution of seismic stations inside the target region, used in the tomographic inversion for Region 1. The thick black lines denote plate boundaries. The coordinate transformation is applied (see the text for details).

Figure 4. The same as Figure 3 but for Region 2.

Figure 5. The same as Figure 3 but for Region 3.

Figure 6. The same as Figure 3 but for Region 4.

Figure 7. The same as Figure 3 but for Region 5.

Figure 8. The same as Figure 3 but for Region 6.

Figure 9. The same as Figure 3 but for Region 7.

Figure 10. The same as Figure 3 but for Region 8.

Figure 11. The same as Figure 3 but for Region 9.

Figure 12. The same as Figure 3 but for Region 10.

Figure 13. The same as Figure 3 but for Region 11.

Figure 14. The same as Figure 3 but for Region 12.

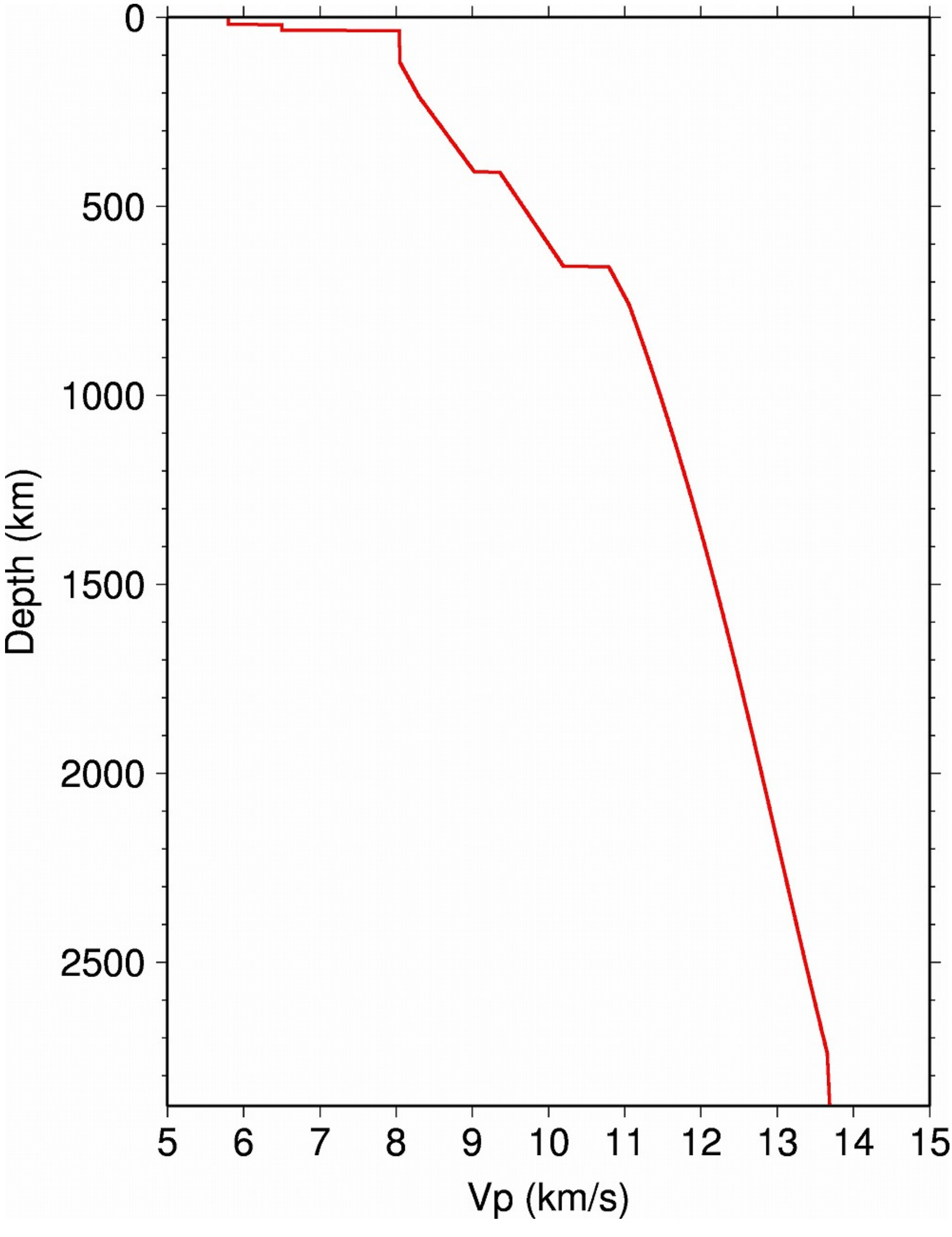

Figure S15. The starting 1-D *P* wave velocity model (IASP91) (Kennett & Engdahl, 1991) adopted for 3-D tomographic inversions.

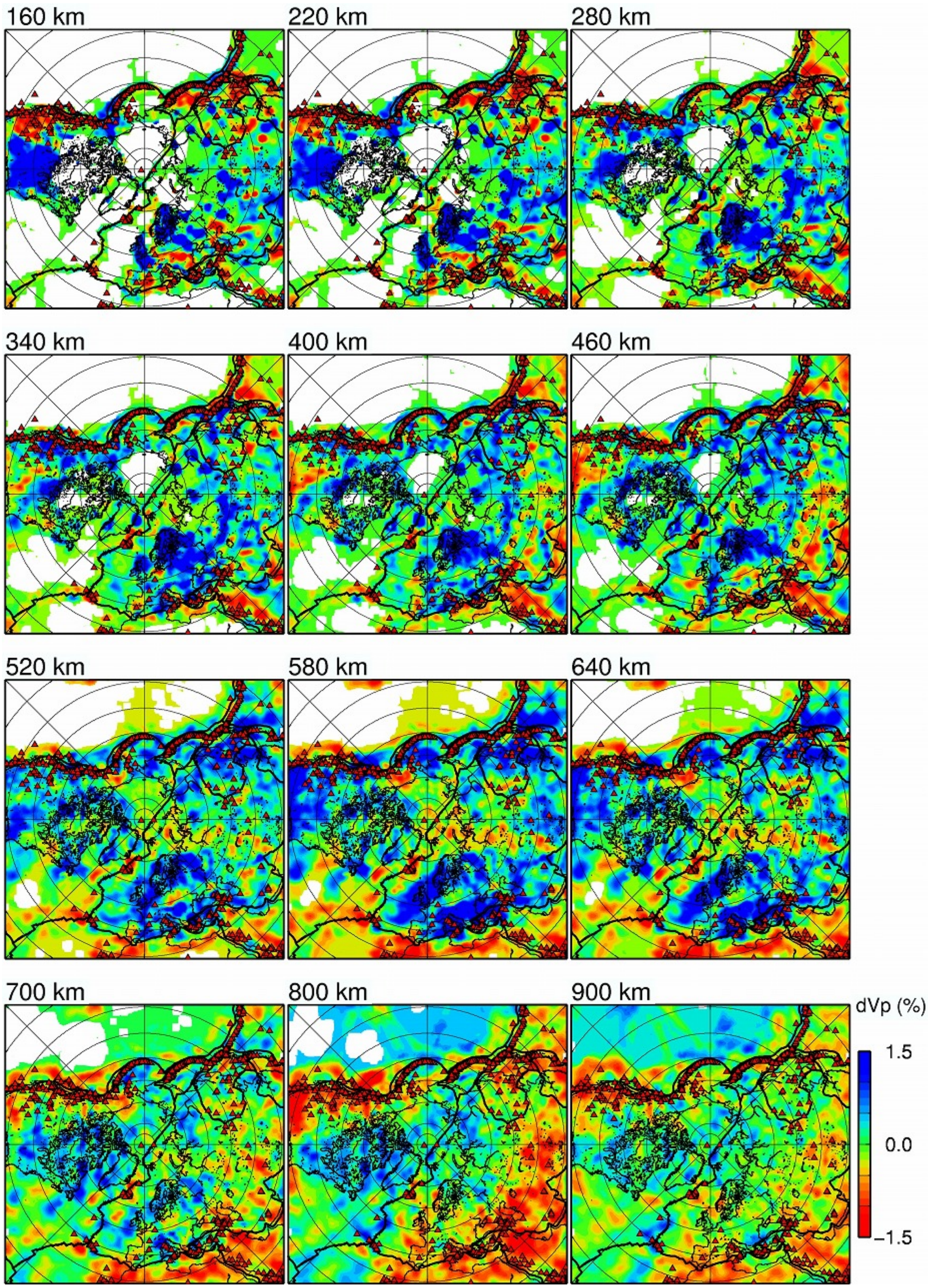

160 km
220 km
280 km
340 km
400 km
460 km
520 km
580 km
640 km
700 km
800 km
900 km
dVp (%)
1.5
0.0
–1.5

Figure S16.

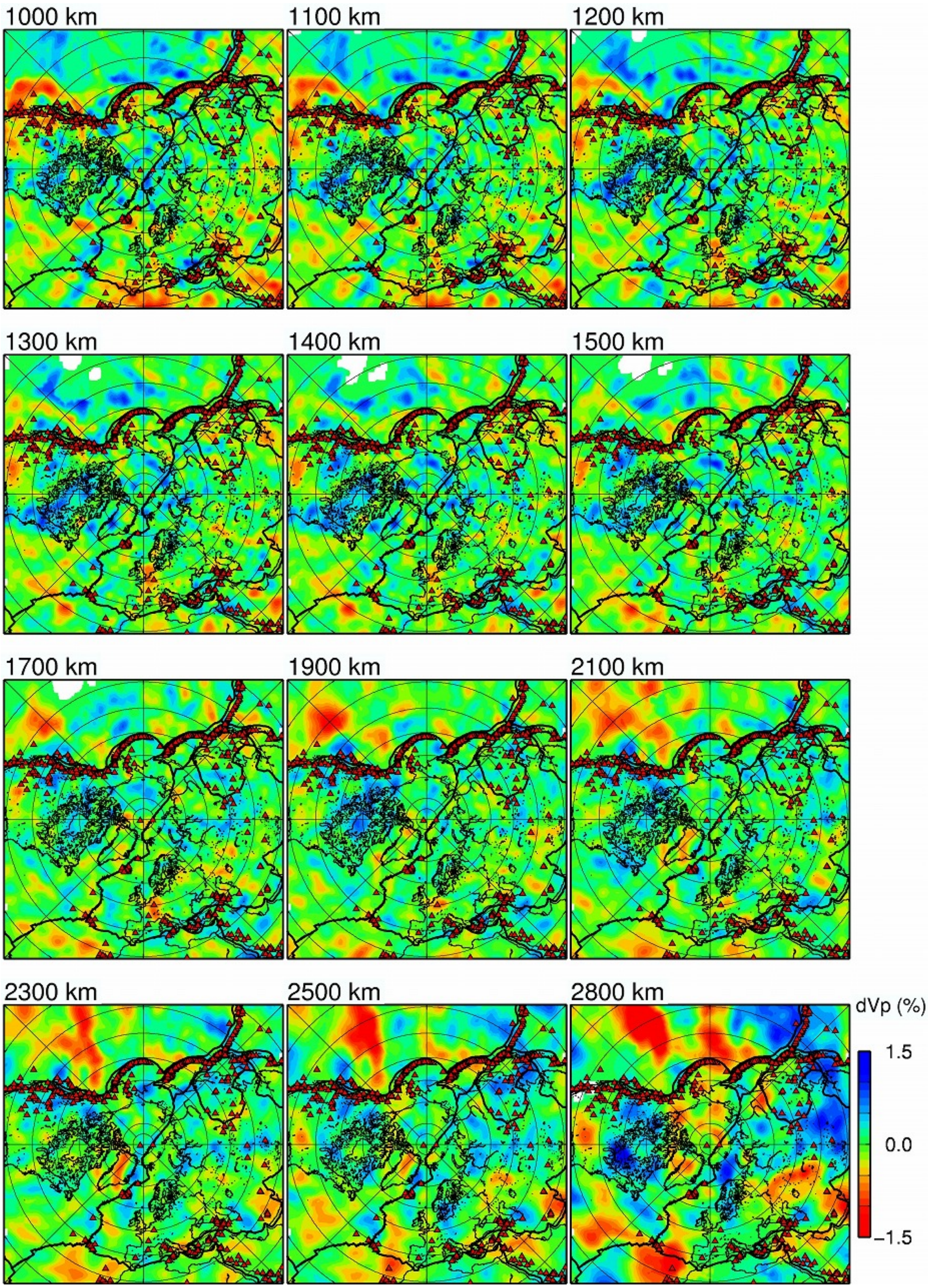

Figure S16. (continued)

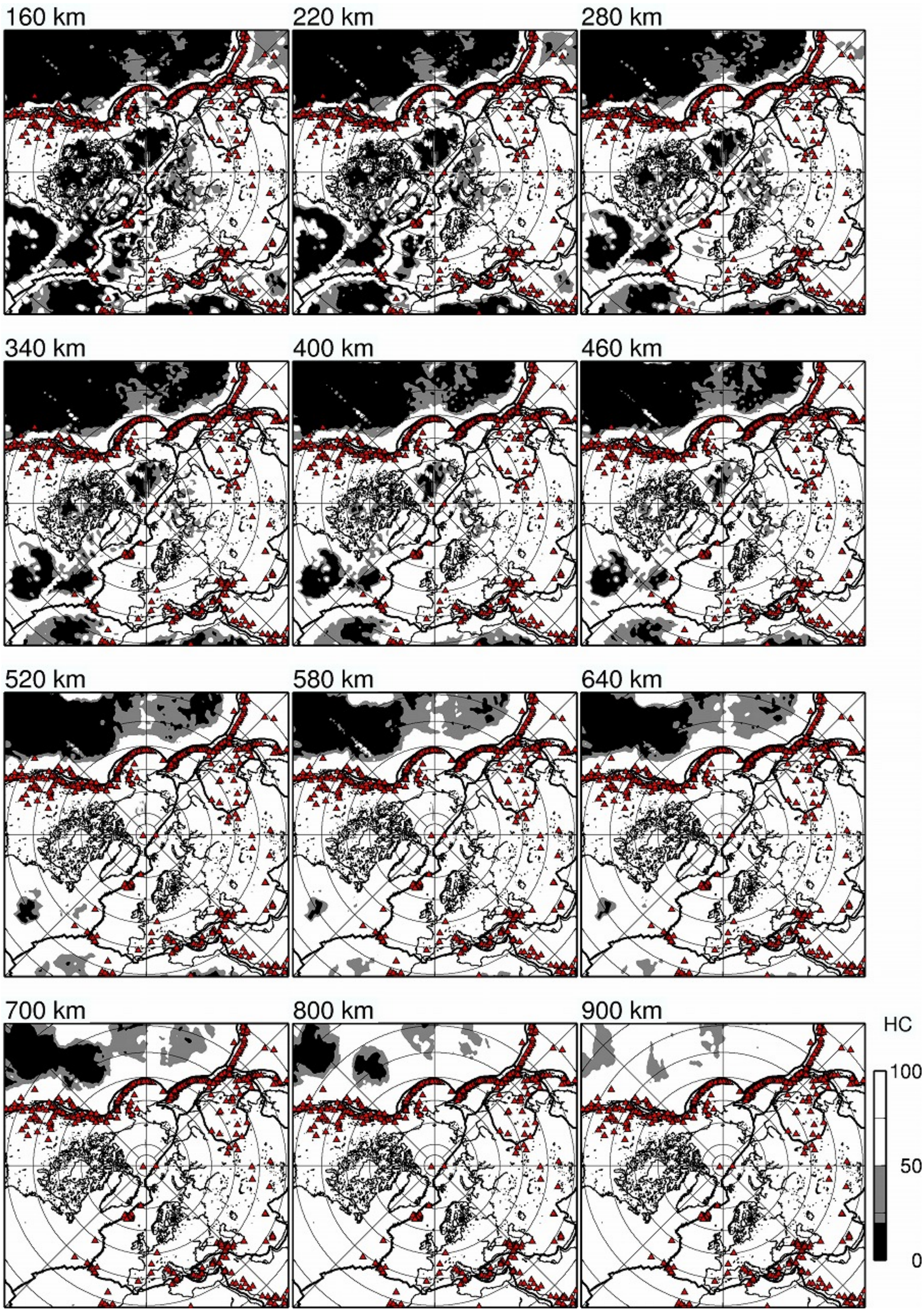
160 km
220 km
280 km
340 km
400 km
460 km
520 km
580 km
640 km
700 km
800 km
900 km
HC
100
50
0

Figure S17.

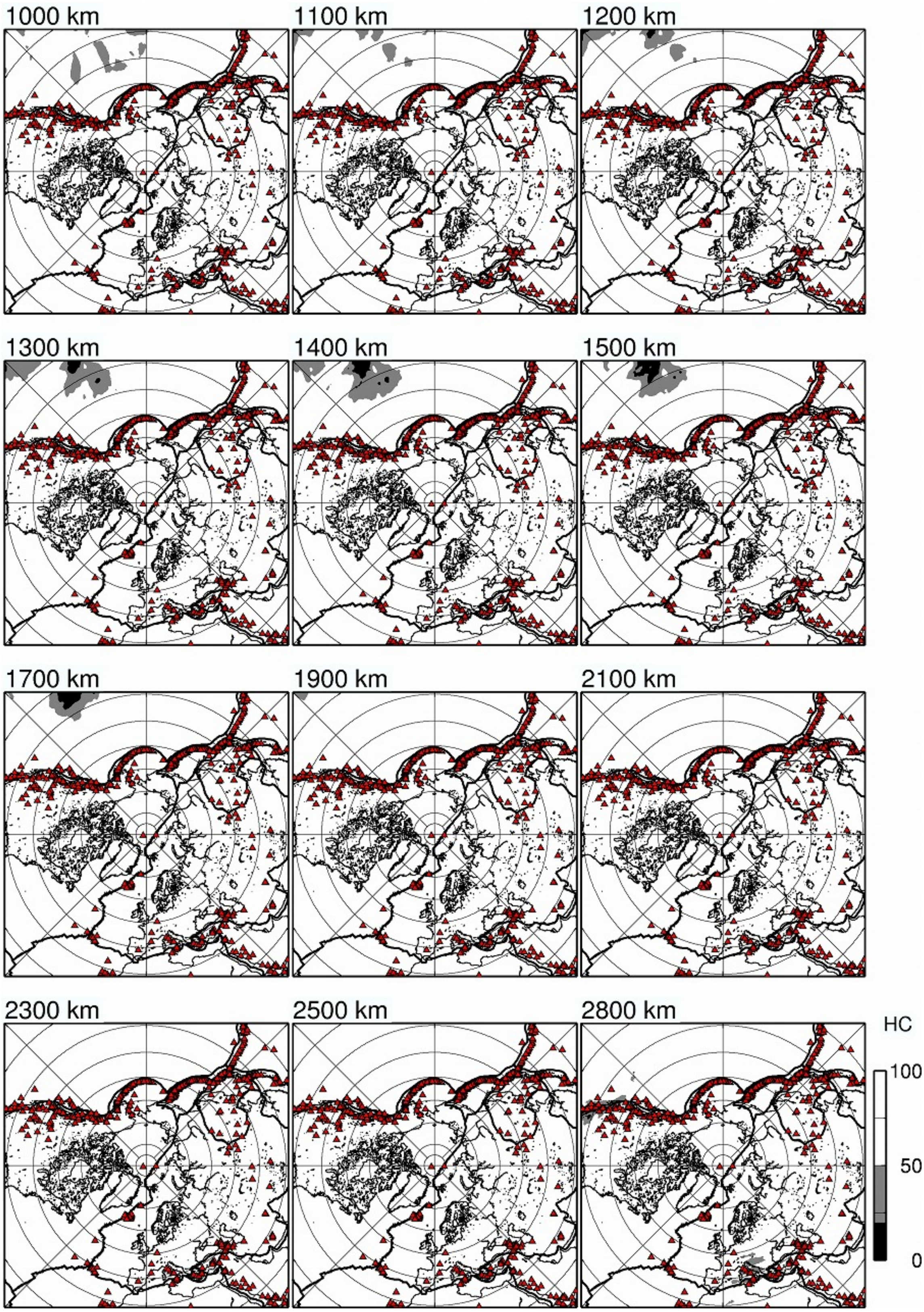

Figure S17. (continued)

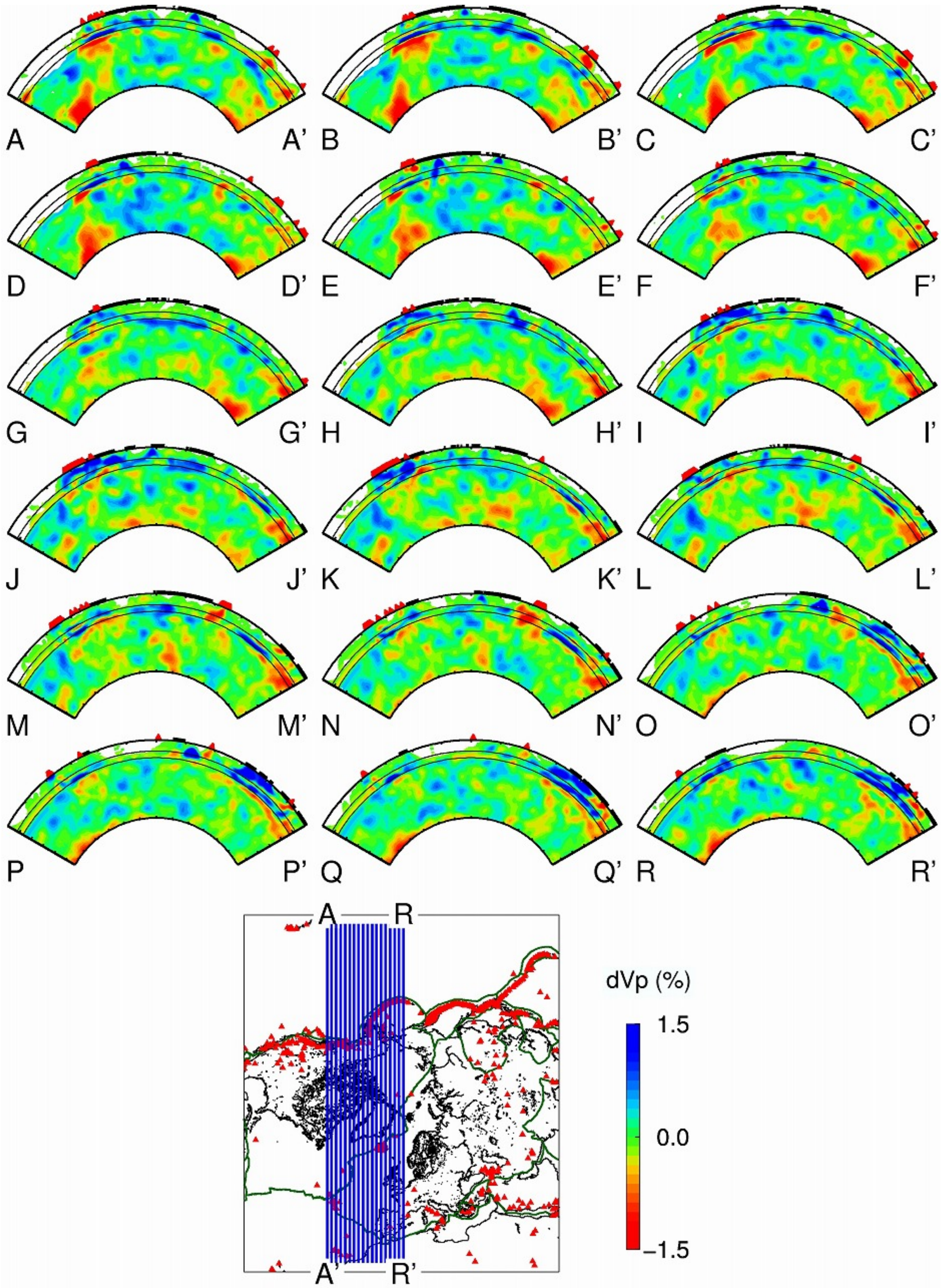

Figure S18.

Figure S16. Map views of Vp tomography. The layer depth is shown above each map. The blue and red colors denote high and low Vp perturbations, respectively, whose scale (in %) is shown on the right. Areas with average hit counts < 20 are masked in white. Red triangles: active volcanoes; thick black lines: plate boundaries.

Figure S17. Map views of average ray hit count (HC). The layer depth is shown above each map. The HC scale is shown on the right. The areas in black color with hit HC < 20 are masked in the resulting tomographic images. Red triangles: active volcanoes; thick black lines: plate boundaries.

Figure S18. Vertical cross sections of Vp tomography along 18 profiles beneath North America and Greenland as shown on the inset map. The 410-km and 660-km discontinuities are shown in black solid lines. The thick black lines on the surface denote land areas. Active volcanoes within a ±2° width of each profile are shown as red triangles. Other labels are the same as those in Figure 3.

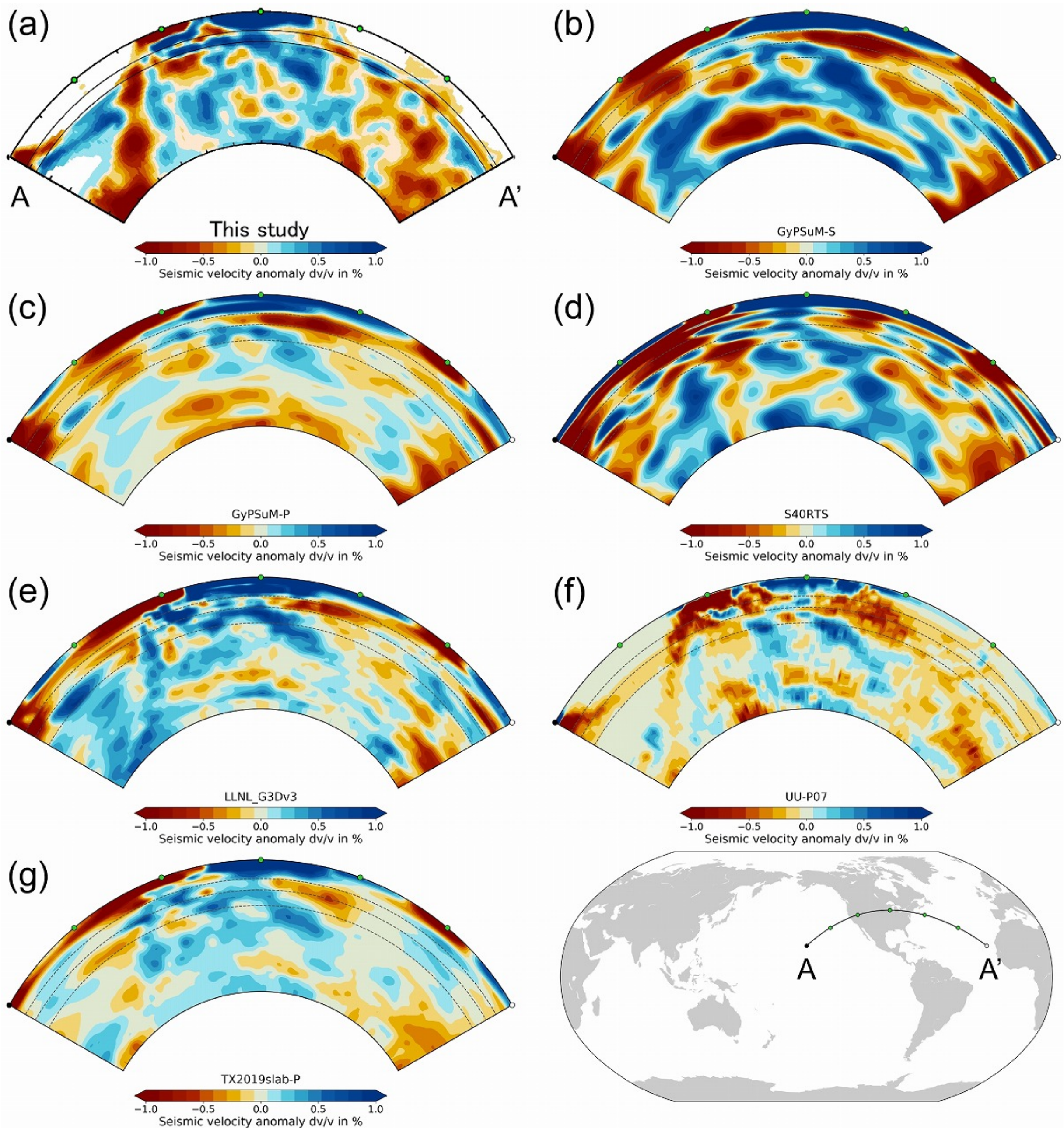

Figure S19. Comparison of tomographic models along A-A' profile on the inset map. **(a)** This study, **(b)** GyPSuM-S (Simmons et al., 2010), **(c)** GyPSuM-P (Simmons et al., 2010), **(d)** S40RTS (Ritsema et al., 2011), **(e)** LLNL_G3Dv3 (Simmons et al., 2012), **(f)** UU-P07 (Amaru, 2007), and **(g)** TX2019slab-P (Lu et al., 2019). The same color scale is adopted for all models. The cross sections **(b)−(g)** are generated at the SubMachine site (https://www.earth.ox.ac.uk/~smachine/cgi/index.php) (Hosseini et al., 2018).

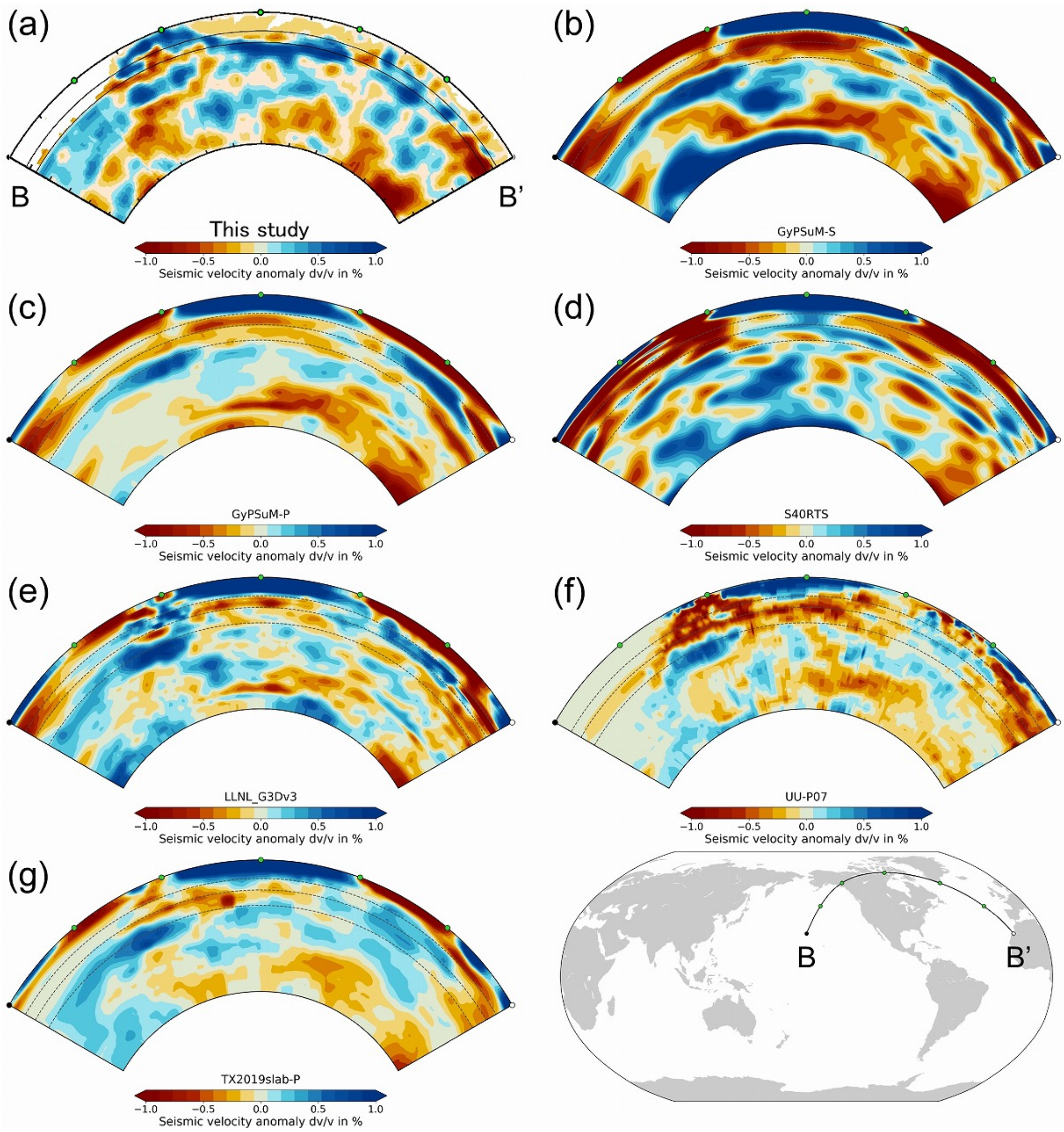

Figure S20. The same as Figure S19 but along B-B' profile on the inset map.

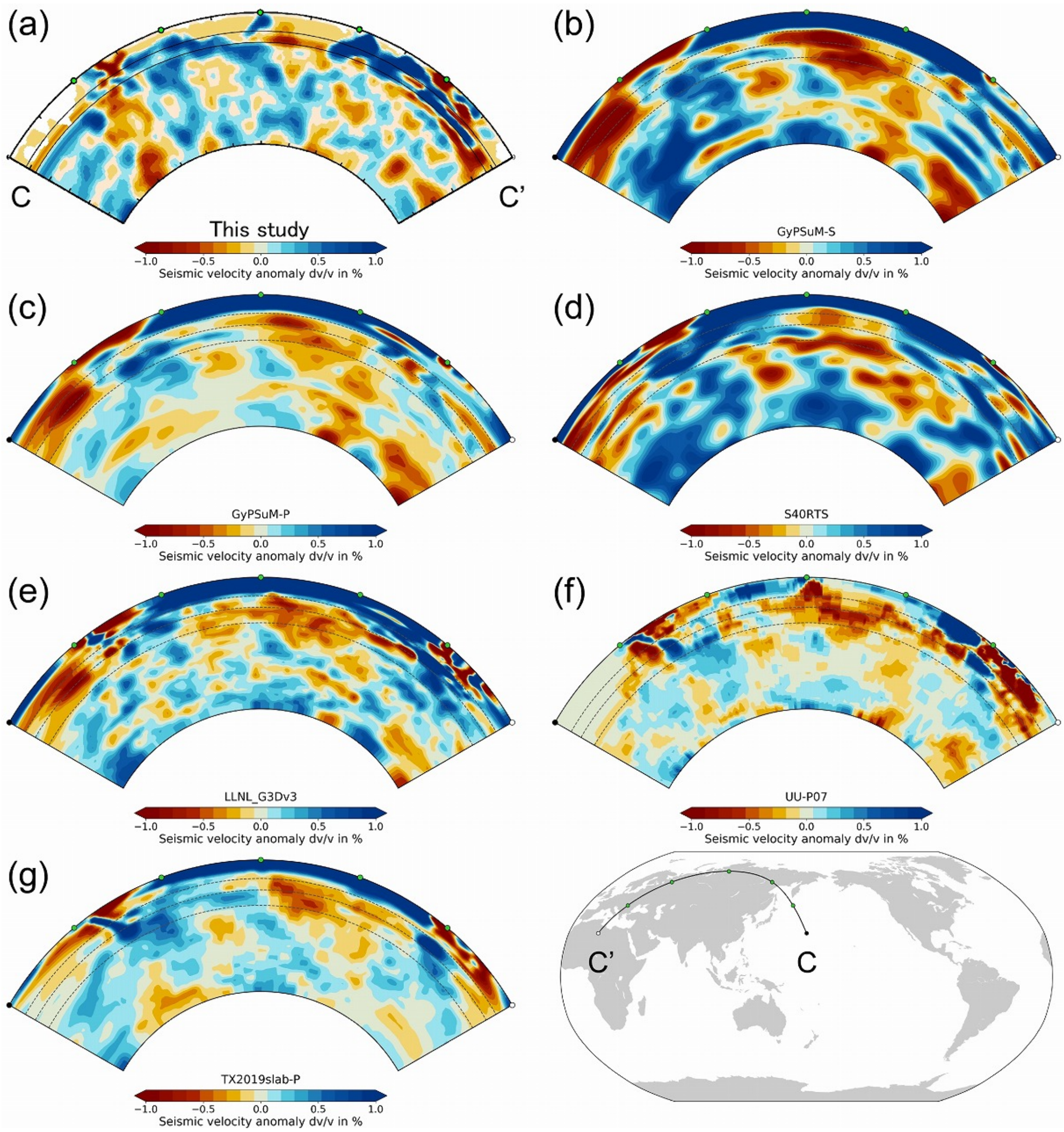

Figure S21. The same as Figure S19 but along B-B’ profile on the inset map.

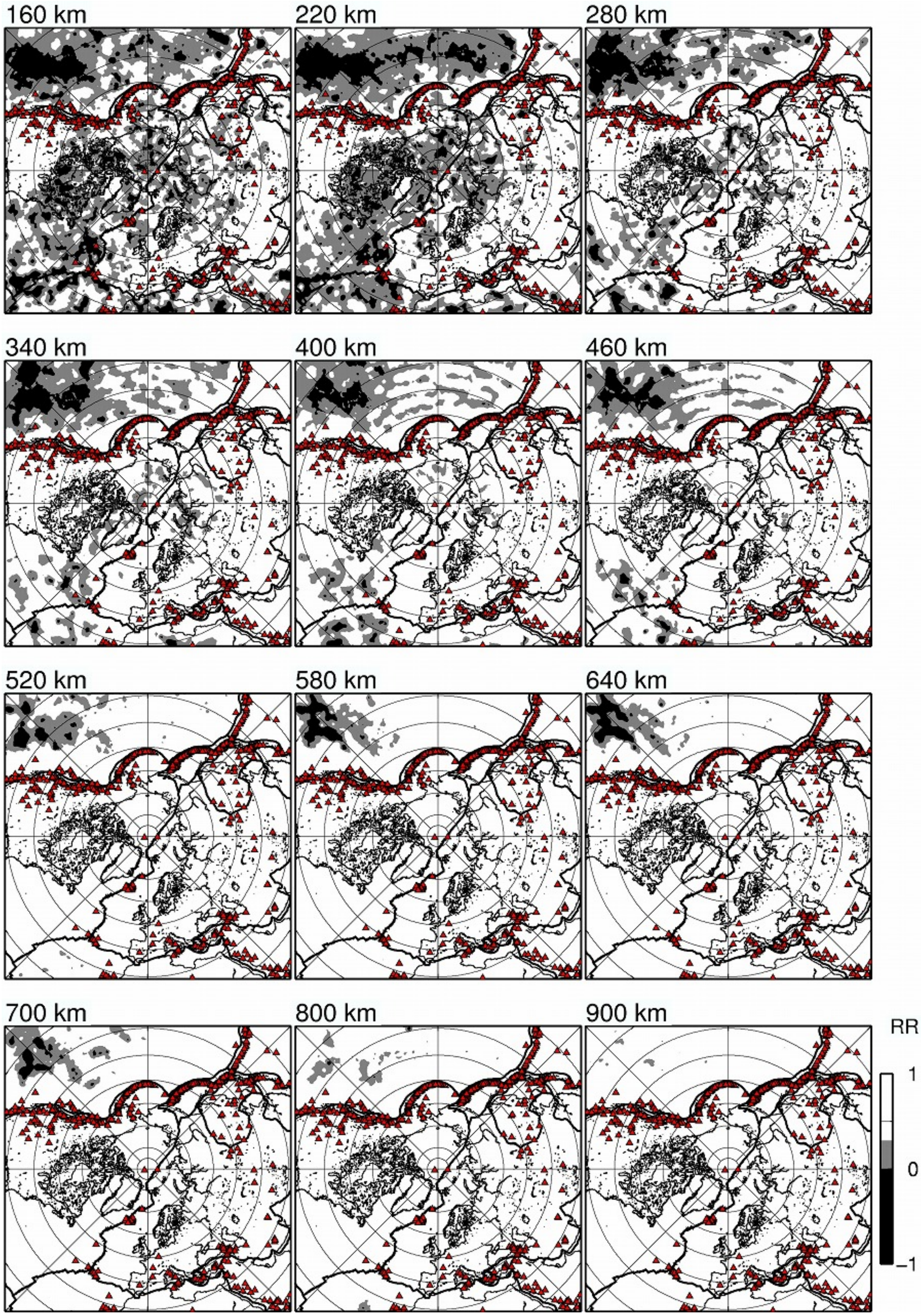
160 km
220 km
280 km
340 km
400 km
460 km
520 km
580 km
640 km
700 km
800 km
900 km
RR
1
0
−1

Figure S22.

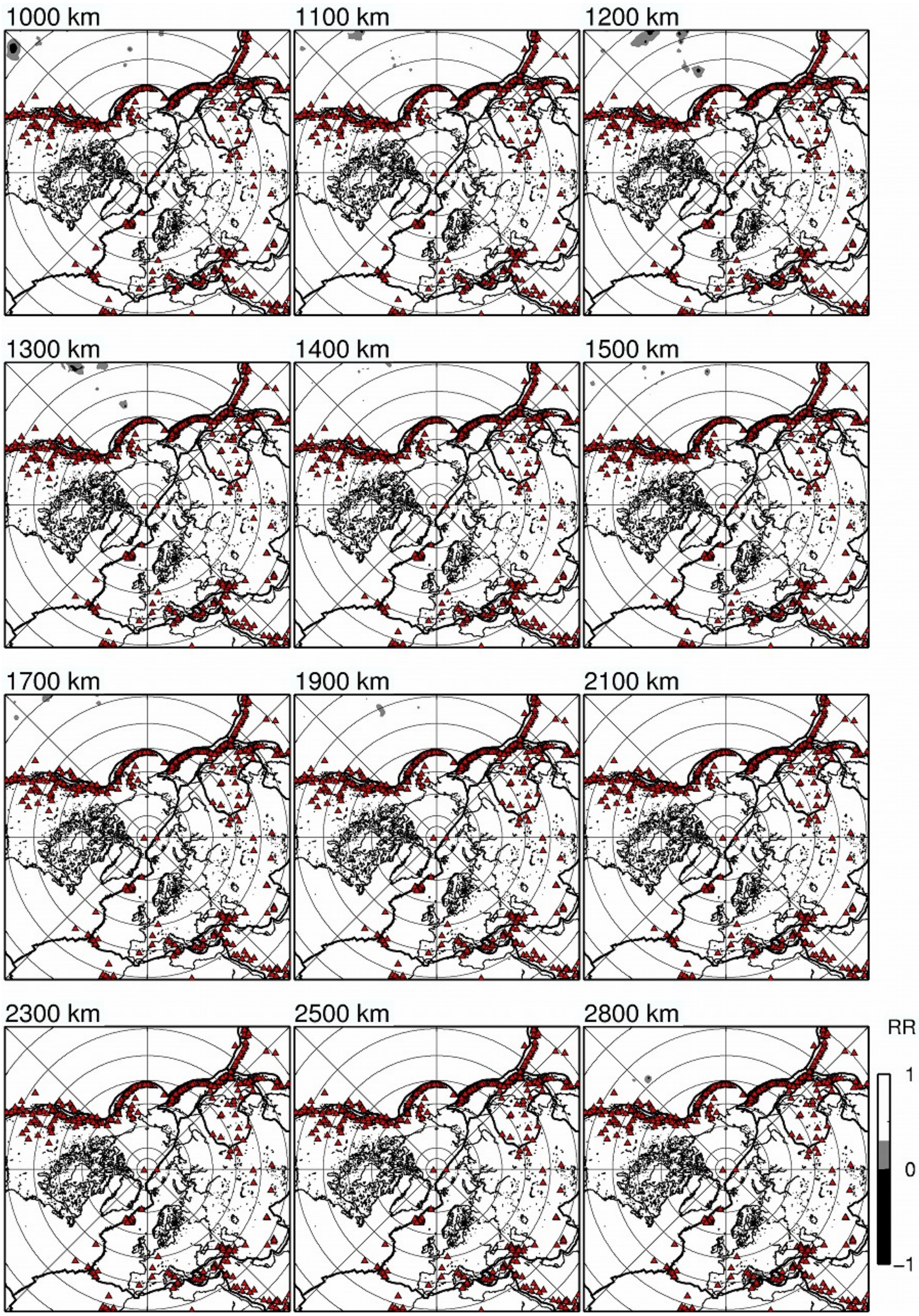

Figure S22. (continued)

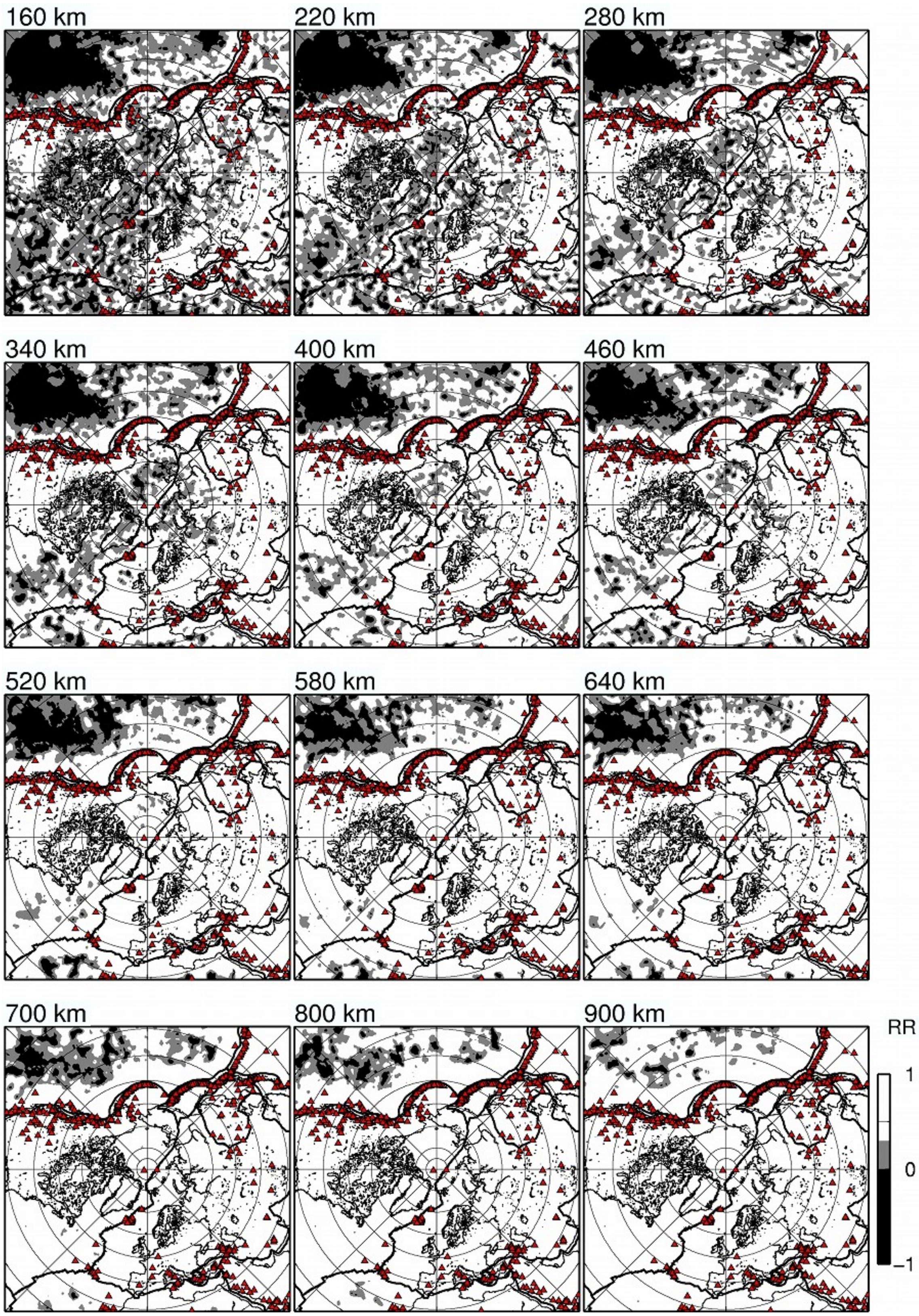
160 km
220 km
280 km
340 km
400 km
460 km
520 km
580 km
640 km
700 km
800 km
900 km
RR
1
0
−1

Figure S23.

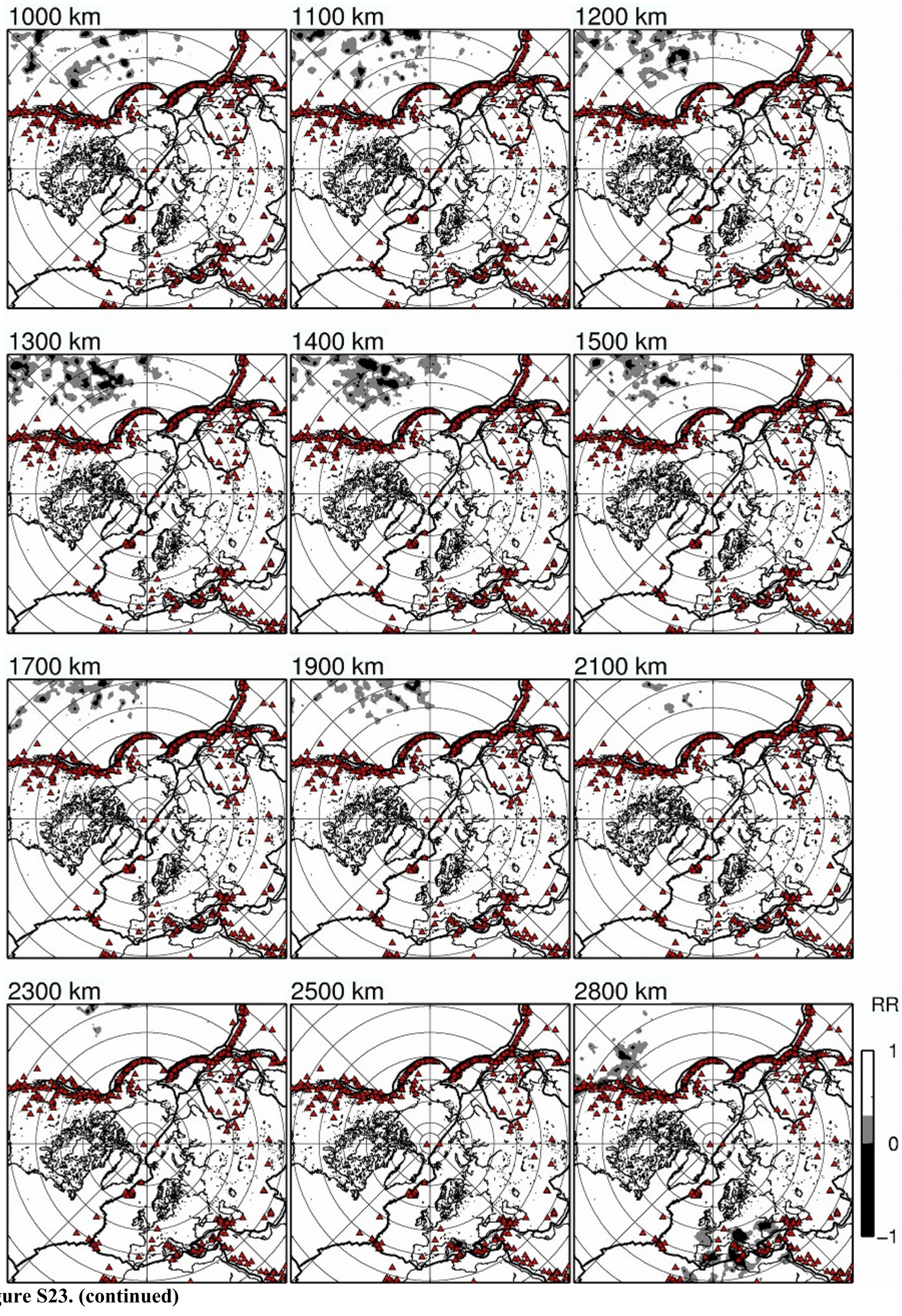

Figure S23. (continued)

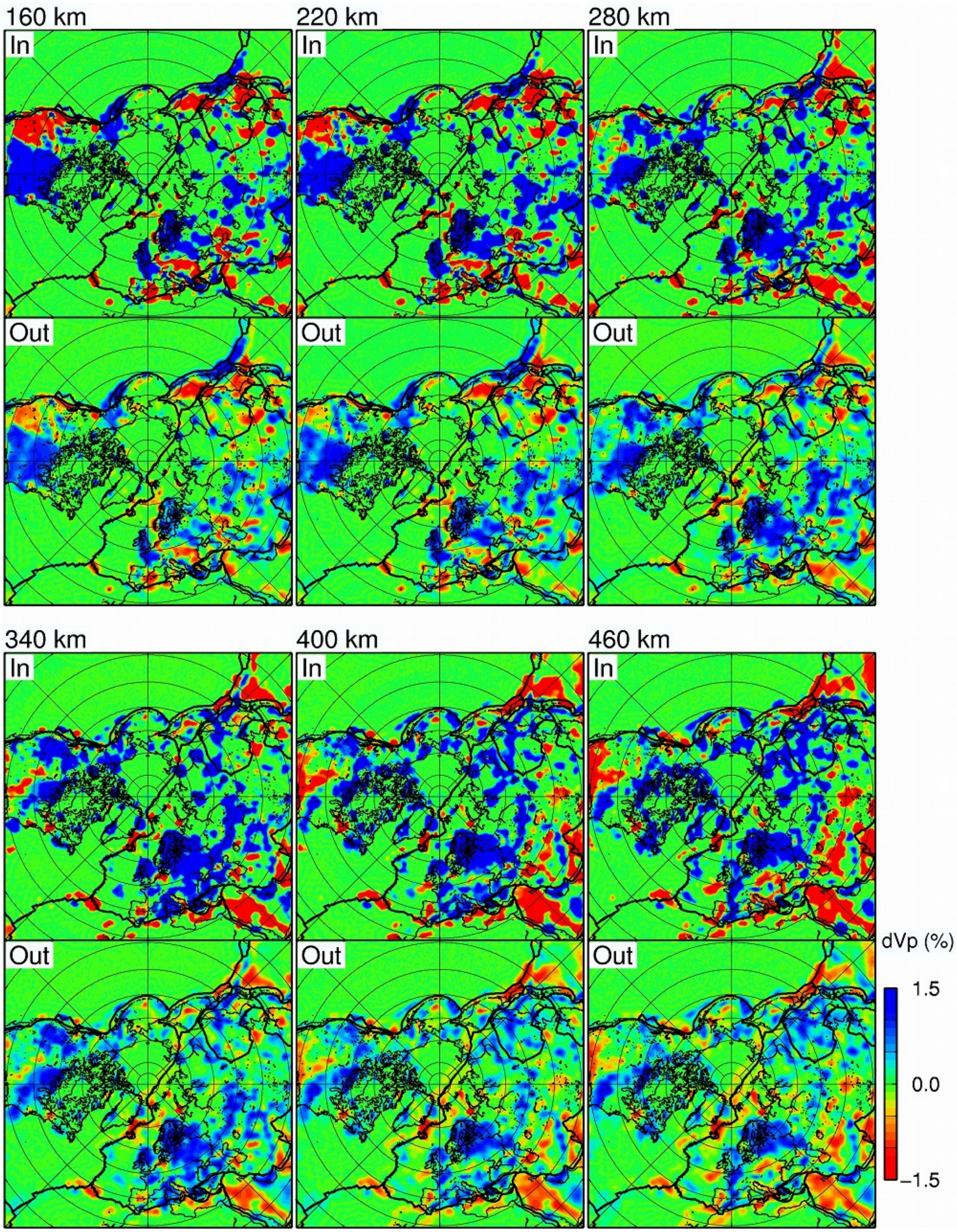

Figure S24.

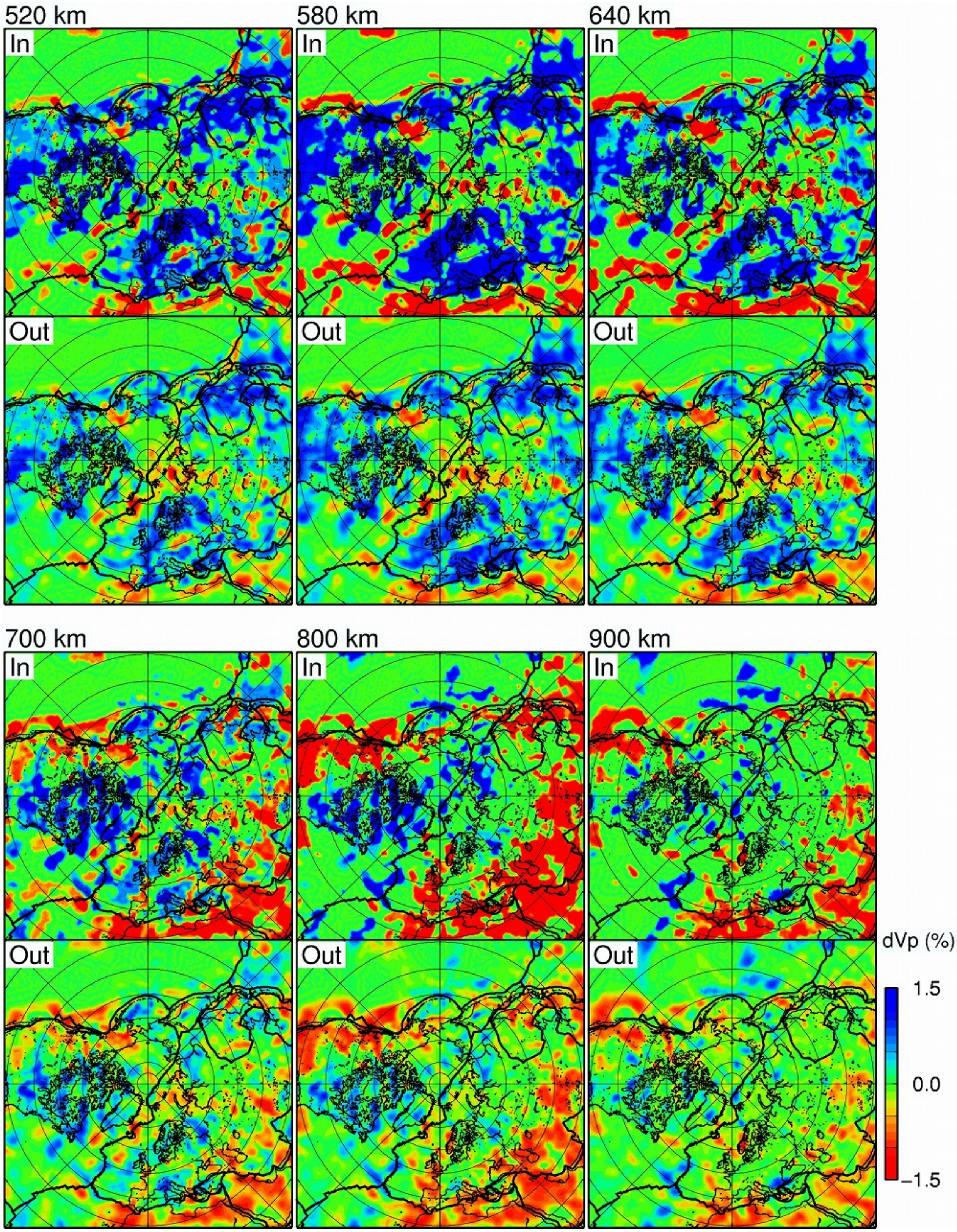

Figure S24. (continued)

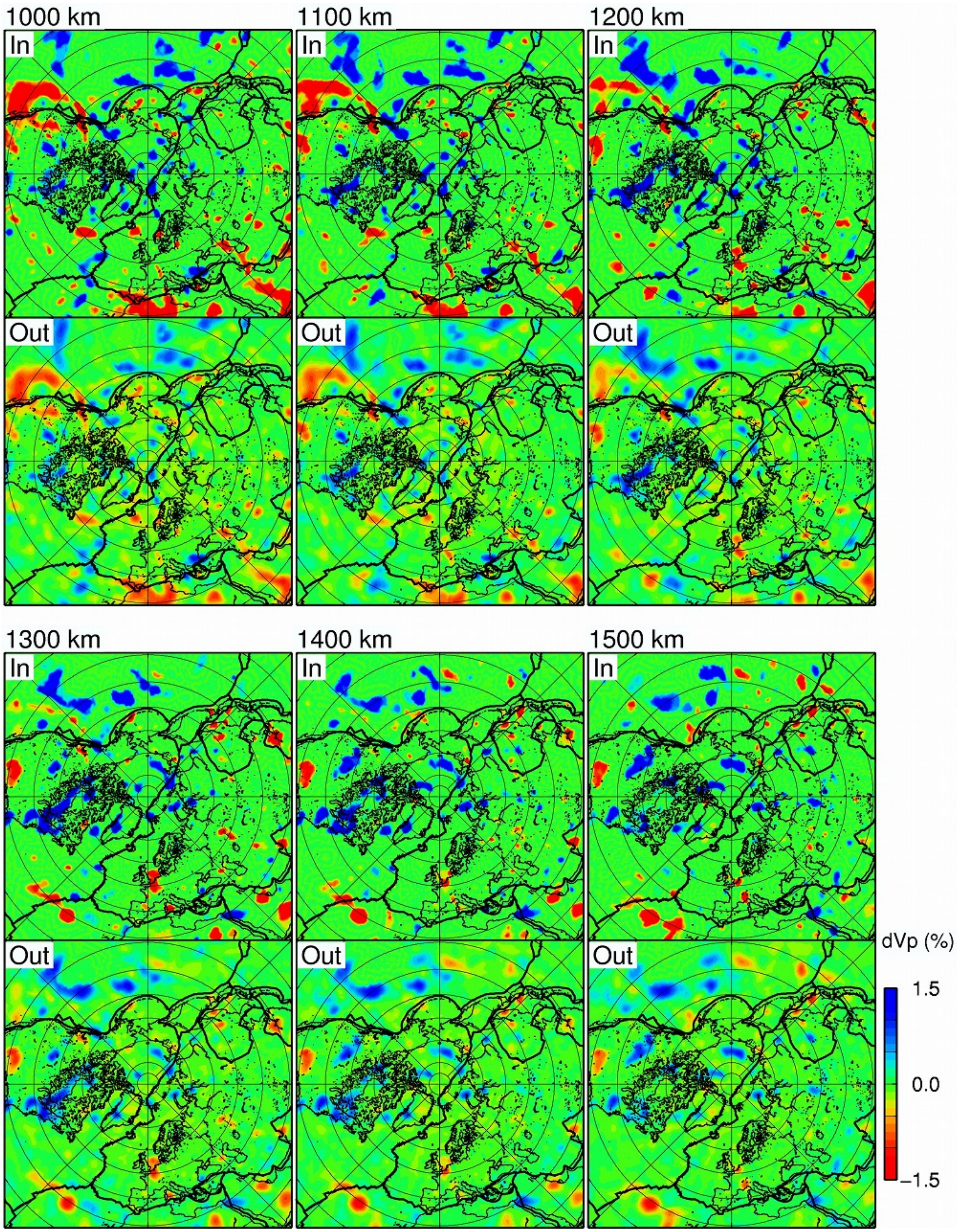

Figure S24. (continued)

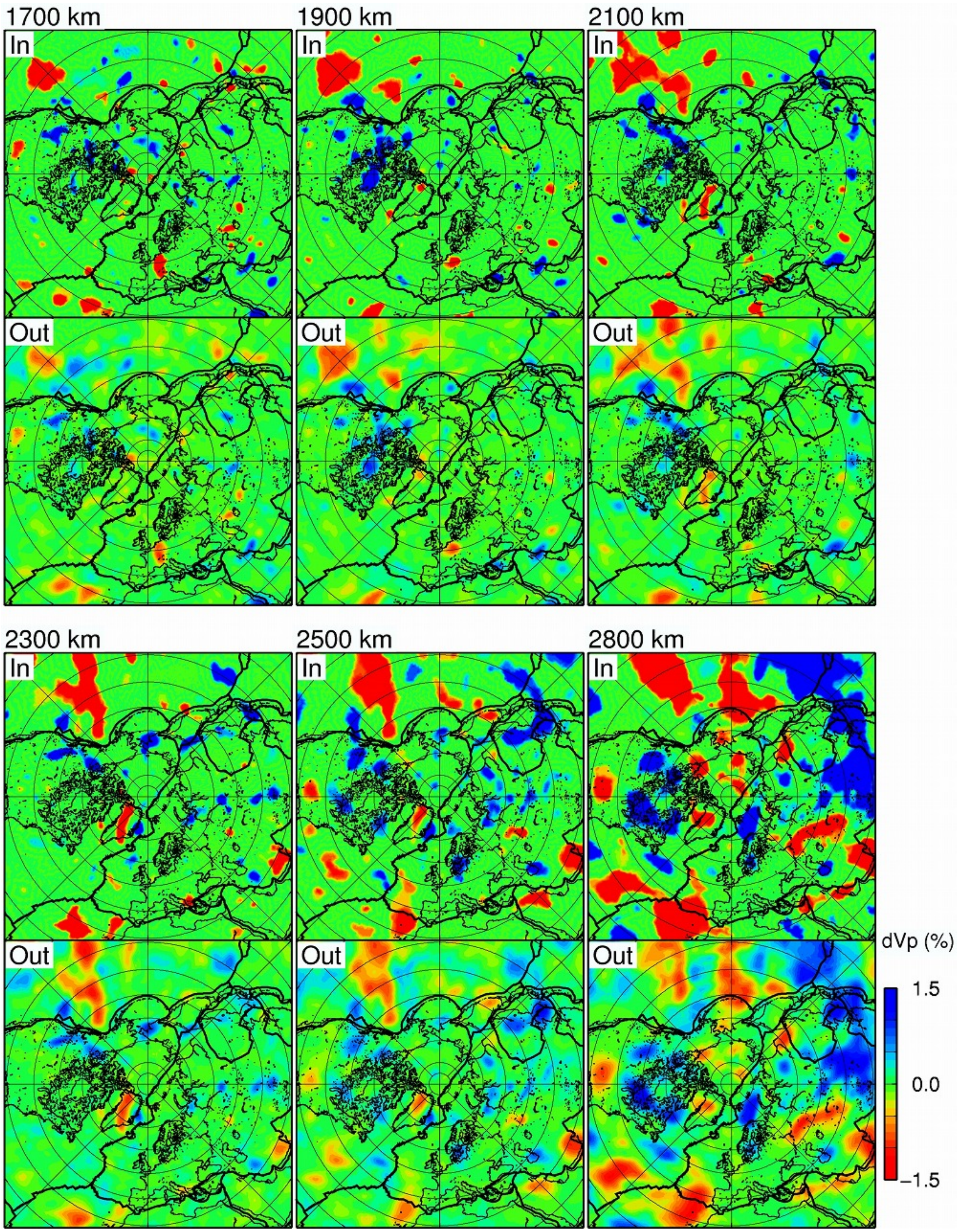

Figure S24. (continued)

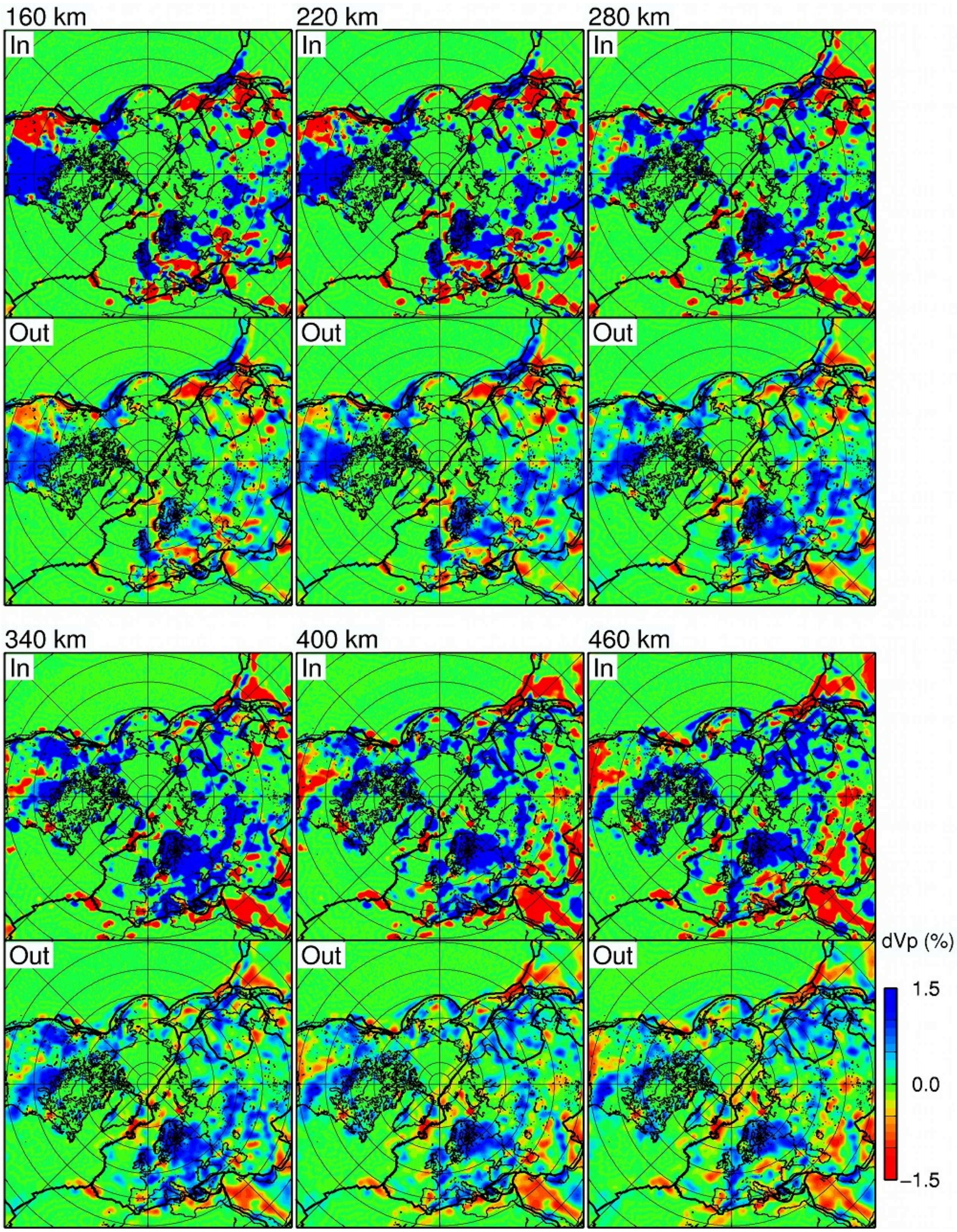

Figure S25.

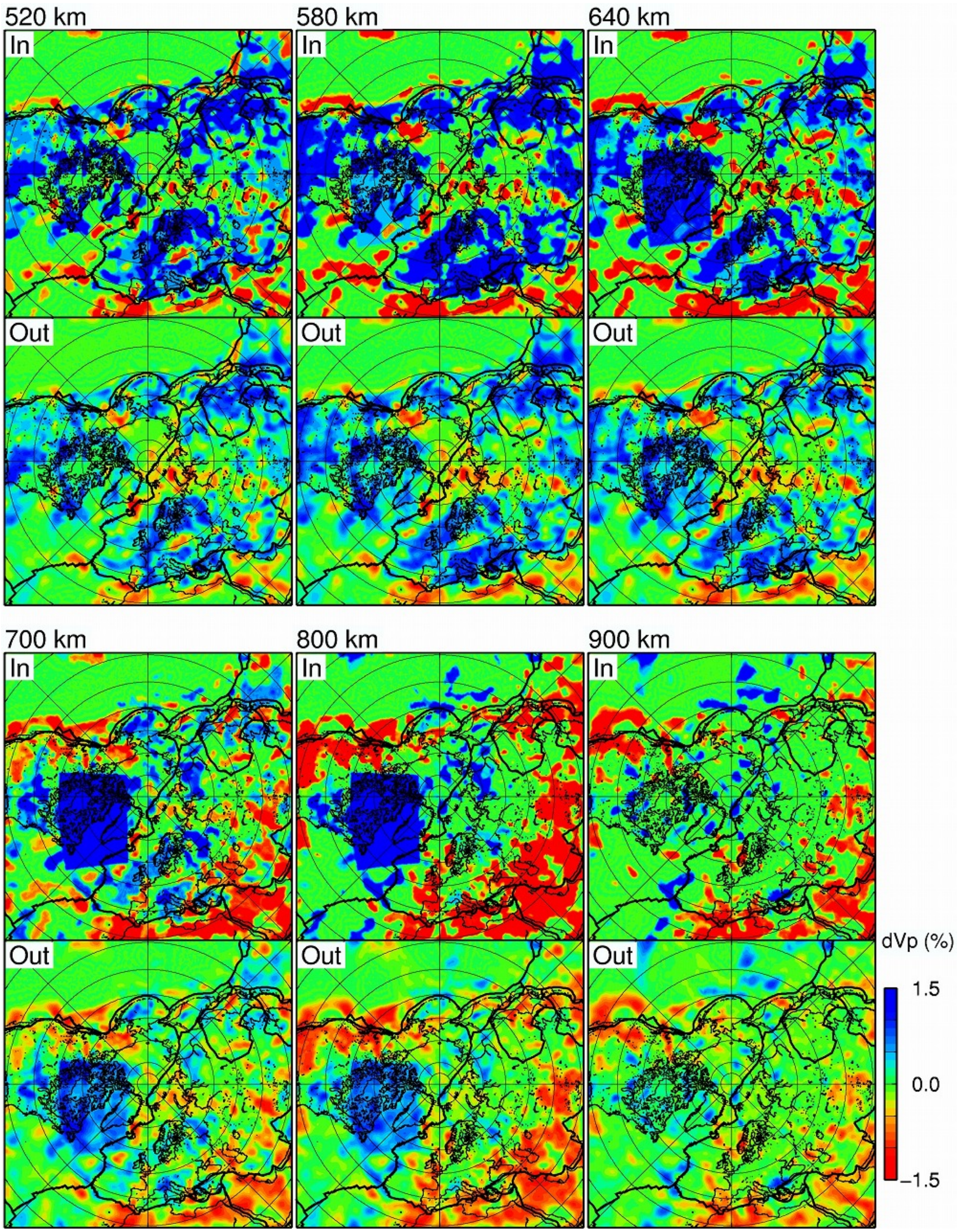

Figure S25. (continued)

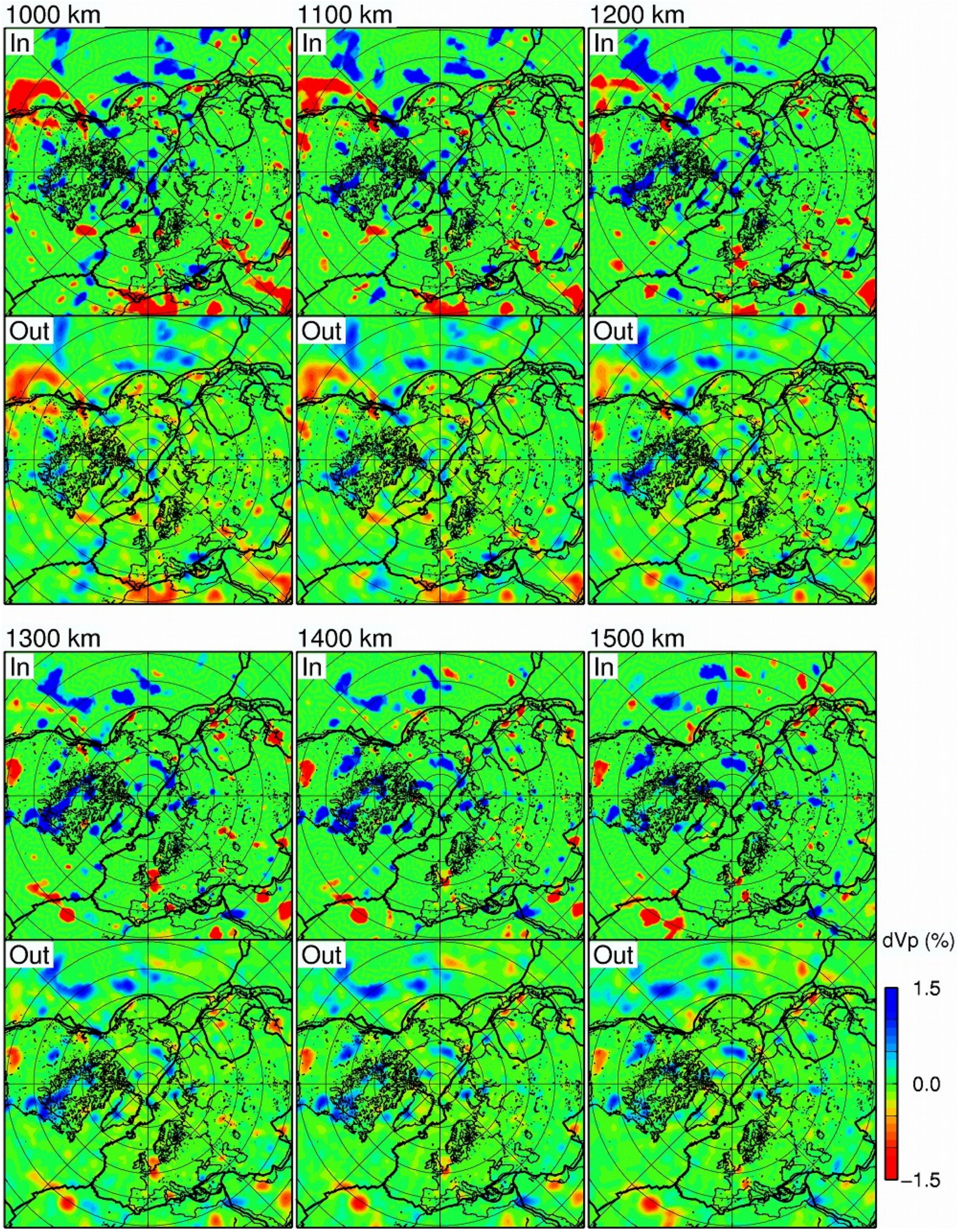

Figure S25. (continued)

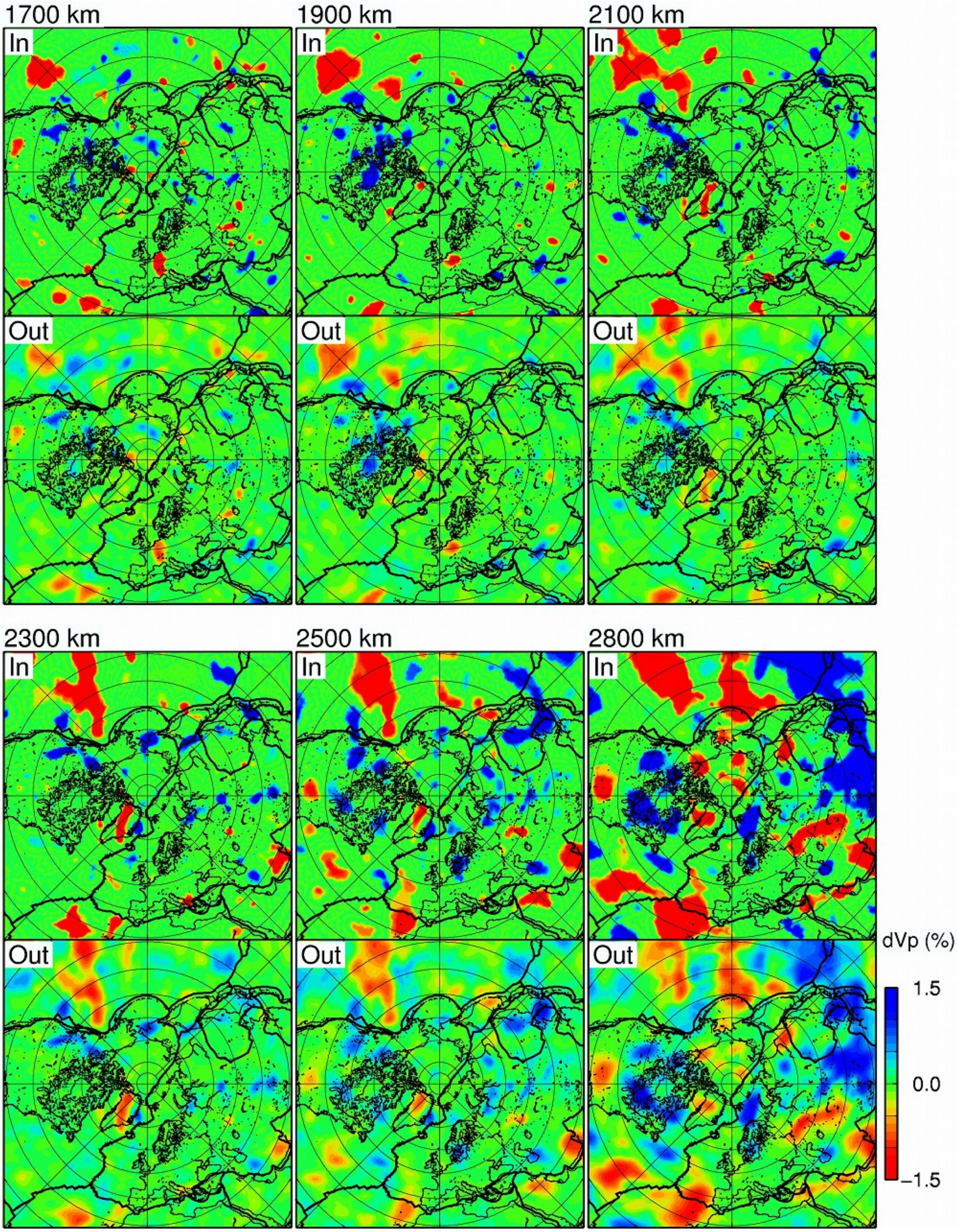

Figure S25. (continued)

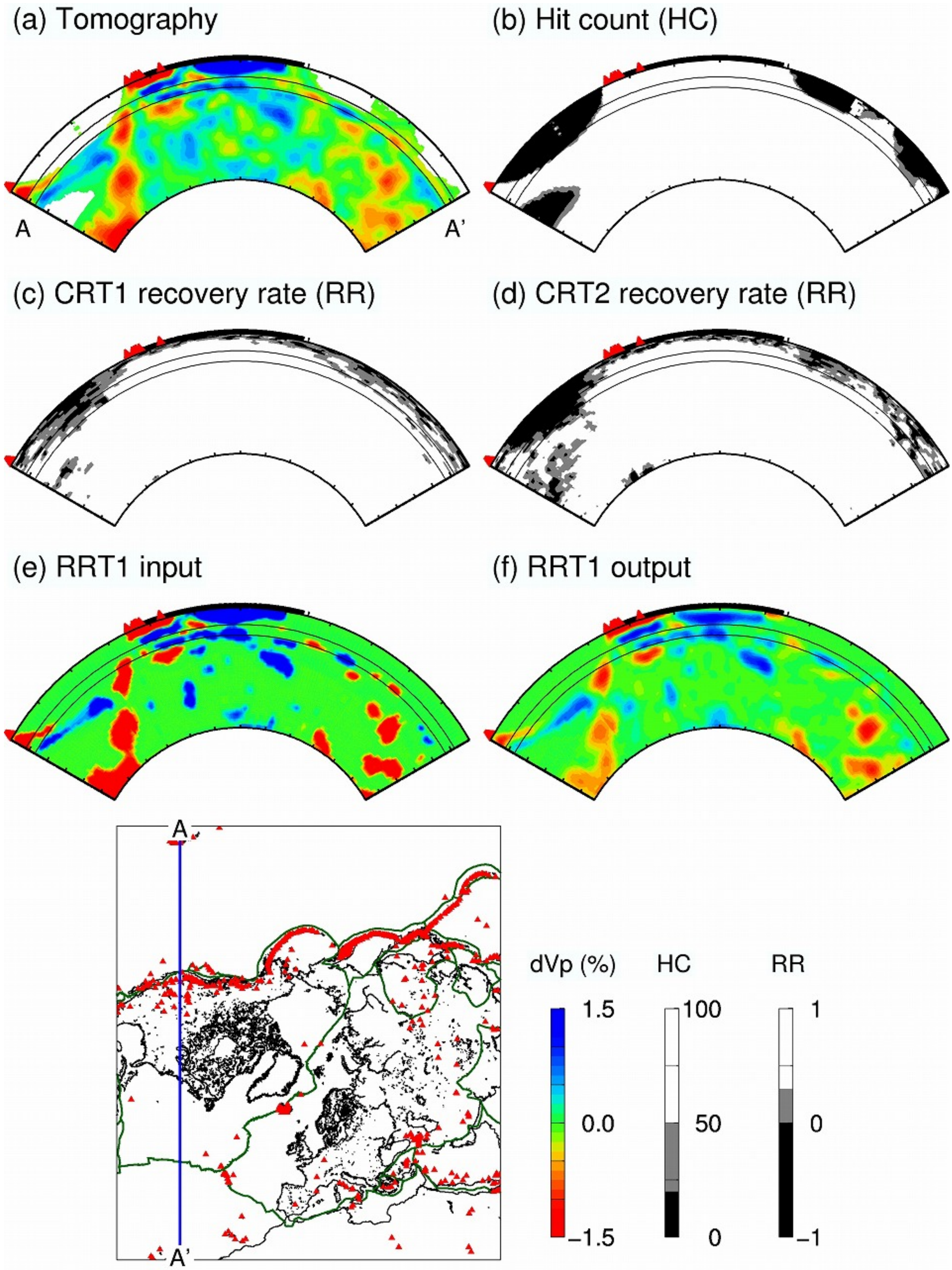
(a) Tomography
(b) Hit count (HC)
A
A'
(c) CRT1 recovery rate (RR)
(d) CRT2 recovery rate (RR)
(e) RRT1 input
(f) RRT1 output
A
A'
dVp (%)
HC
RR
1.5
0.0
−1.5
100
50
0
1
0
−1

Figure S26.

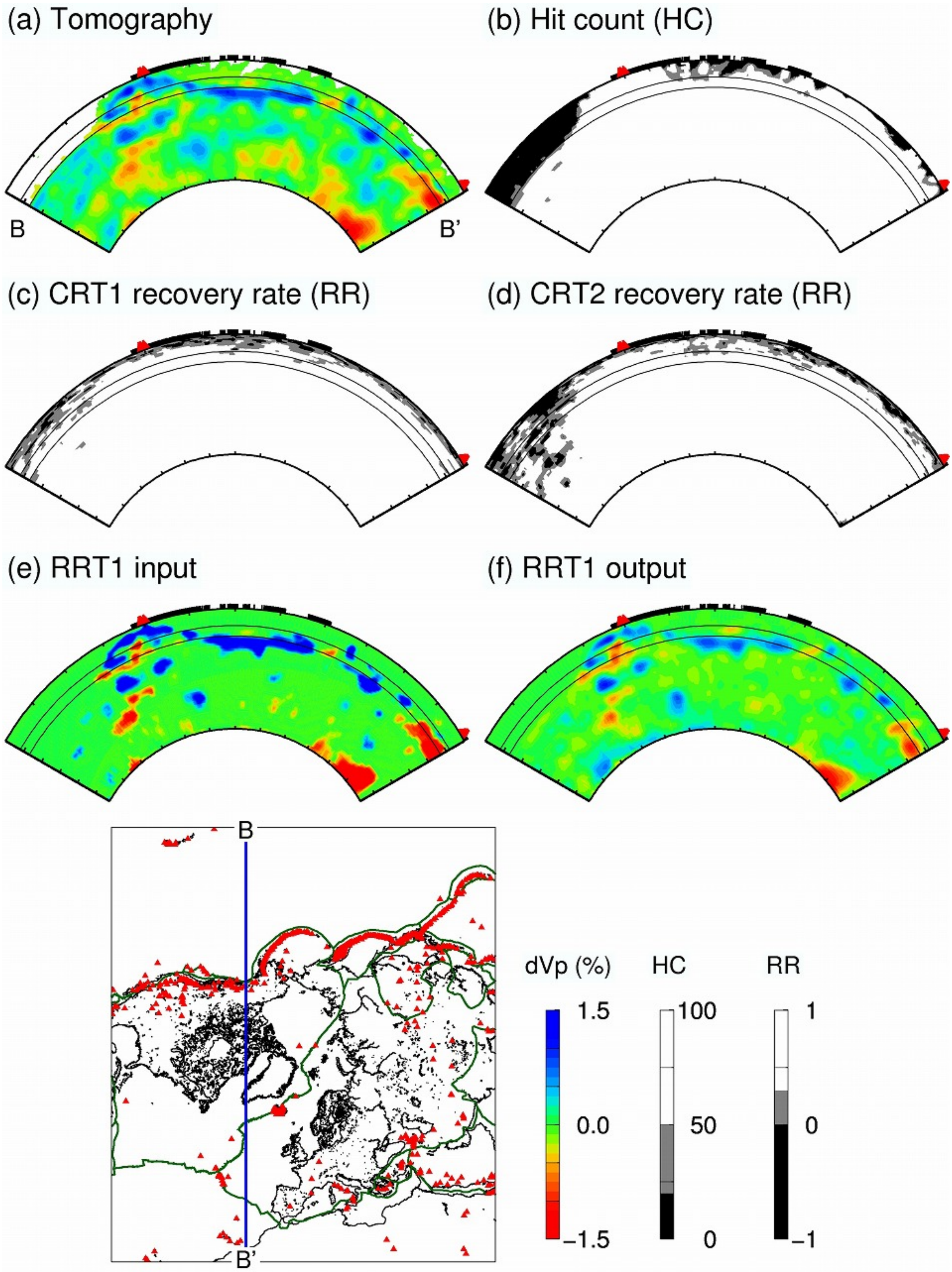
(a) Tomography
B
B'
(b) Hit count (HC)
(c) CRT1 recovery rate (RR)
(d) CRT2 recovery rate (RR)
(e) RRT1 input
(f) RRT1 output
B
B'
dVp (%)
1.5
0.0
–1.5
HC
100
50
0
RR
1
0
–1

Figure S27.

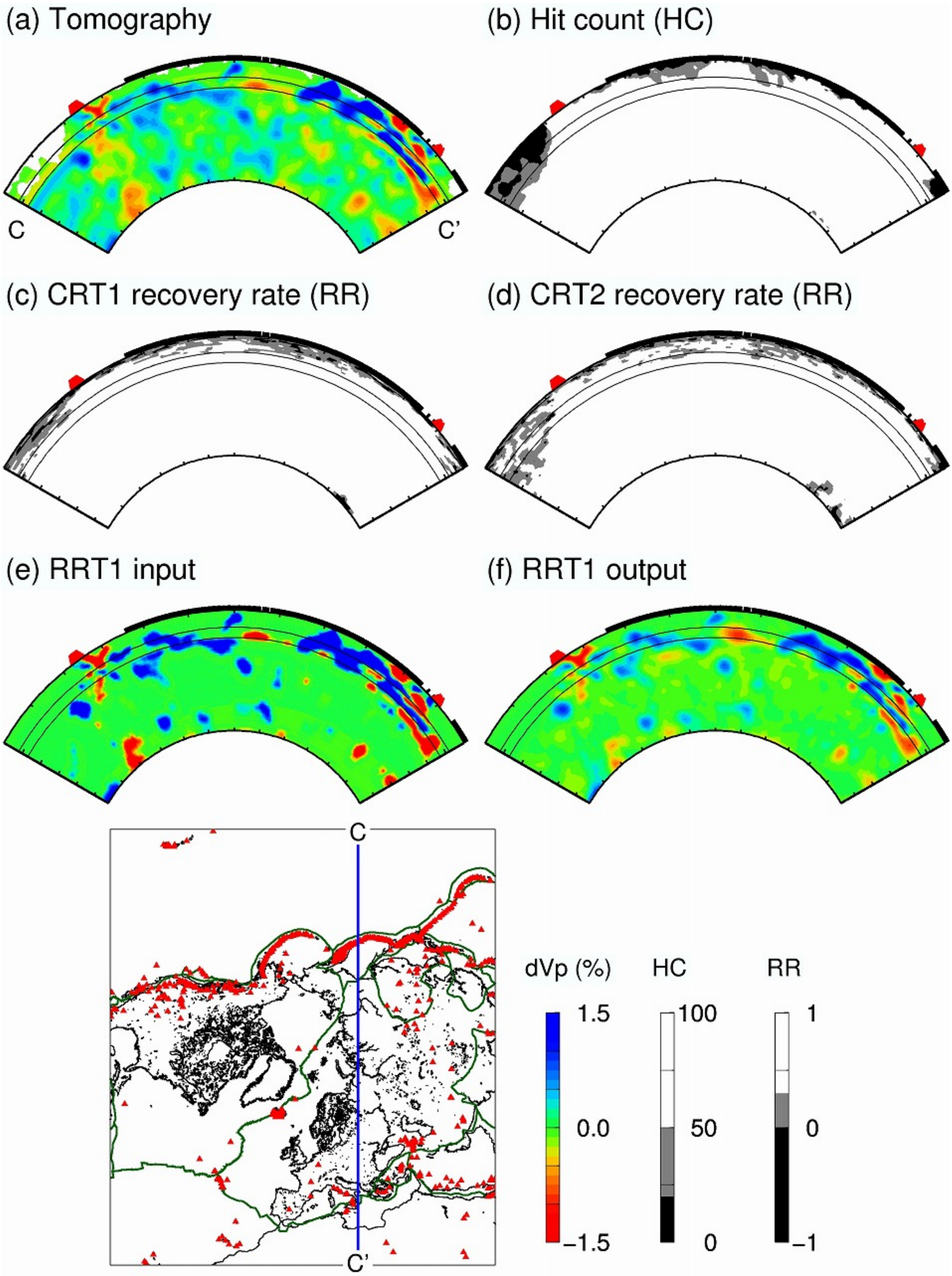

(a) Tomography
(b) Hit count (HC)
(c) CRT1 recovery rate (RR)
(d) CRT2 recovery rate (RR)
(e) RRT1 input
(f) RRT1 output
C
C'
dVp (%)
1.5
0.0
−1.5
HC
100
50
0
RR
1
0
−1

Figure S28.

Figure S22. Map views of recovery rate (RR) estimated from the result of a checkerboard resolution test with a lateral grid interval of 278 km (a great circle distance of 2.5° on the surface) (CRT1). The layer depth is shown above each map. The RR scale is shown on the right. Red triangles: active volcanoes; thick black lines: plate boundaries.

Figure S23. The same as Figure S22 but estimated from the result of a checkerboard resolution test with a lateral grid interval of 167 km (a great circle distance of 1.5° on the surface) (CRT2).

Figure S24. Map views showing the input model (upper panels) and output results (lower panels) of RRT1. The layer depth is shown above each upper panel. The blue and red colors denote high and low Vp perturbations, respectively, whose scale (in %) is shown on the right. The thick black lines denote plate boundaries.

Figure S25. The same as Figure S24 but for RRT2.

Figure S26. Vertical cross sections along A-A’ profile on the inset map showing **(a)** the obtained tomographic model, **(b)** average ray hit count (HC), **(c)** recovery rate (RR) from the CRT1, **(d)** RR from the CRT2, **(e)** input model of RRT1, and **(f)** output result of RRT1. The 410-km and 660-km discontinuities are shown in black solid lines. The thick black lines on the surface denote land areas. The red triangles denote active volcanoes. Red triangles: active volcanoes; thick green lines on the map: plate boundaries.

Figure S27. The same as Figure S26 but along B-B’ profile on the inset map.

Figure S28. The same as Figure S26 but along C-C’ profile on the inset map.

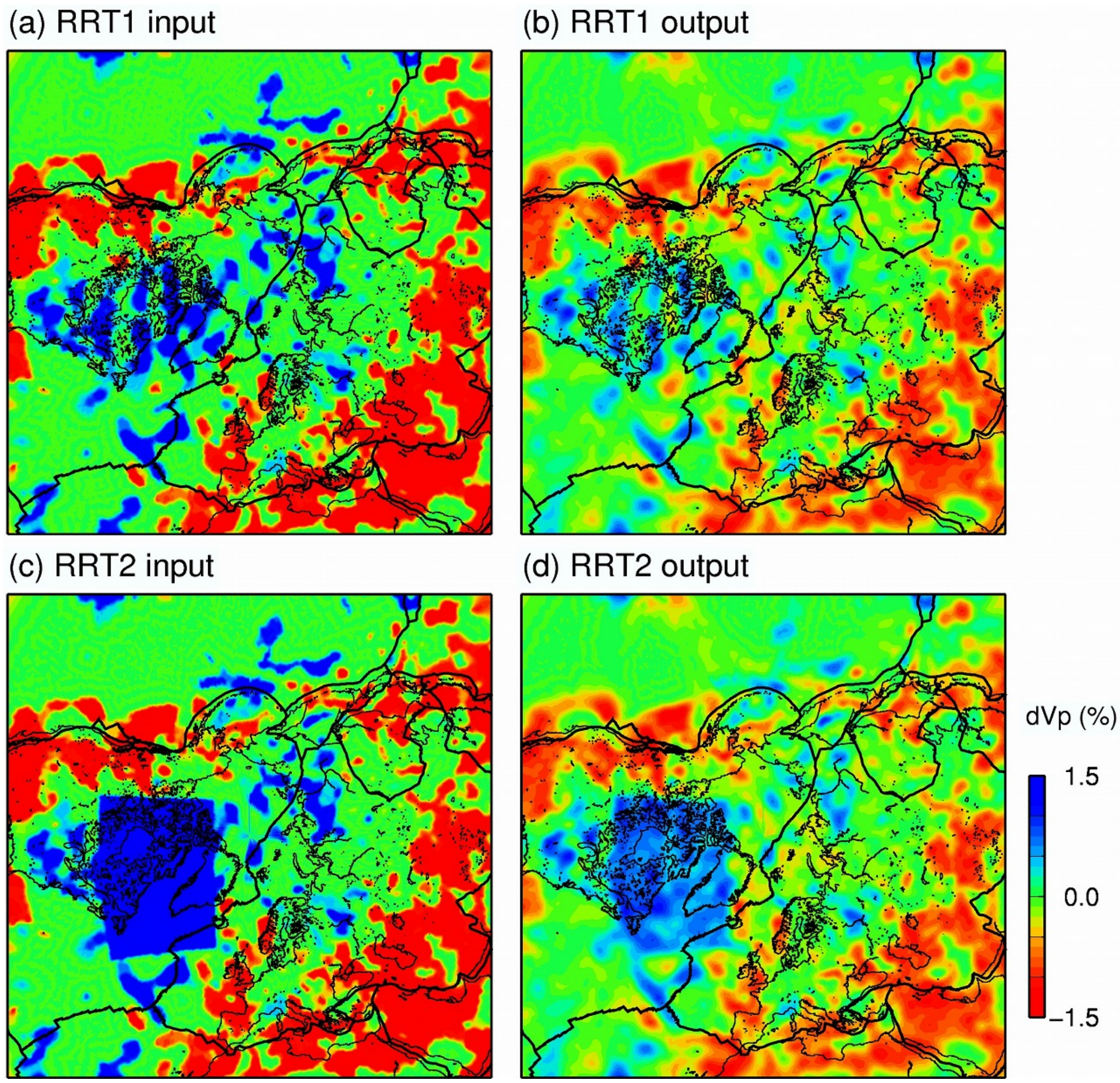

Figure S29. Comparison of the RRT results at a depth of 800 km. **(a)** The RR1 input model, **(b)** the RRT1 output result, **(c)** the RR2 input model, and **(d)** the RRT2 output result. The blue and red colors denote high and low Vp perturbations, respectively, whose scale (in %) is shown on the right. The thick black lines denote plate boundaries.

Table S1. Information on the eight resolution tests conducted by this study.

Region	Center (lon, lat)	Block size	$N_{station}$ (inside)	$N_{station}$ (total)	N_{event}	N_P	N_{pP}	N_{PP}	N_{total}
1	(0.0, 90.0)	0.1° x 5.0 km (in) 1.0° x 20.0 km (out)	923	12,543	17,827	5,762,140	188,989	128,476	6,079,605
2	(-38.461, 90.0)	0.1° x 5.0 km (in) 1.0° x 20.0 km (out)	1,295	12,640	19,045	6,084,018	196,719	130,135	6,410,872
3	(-100.0, 60.0)	0.1° x 5.0 km (in) 1.0° x 20.0 km (out)	4,164	12,612	17,671	5,738,009	190,145	129,393	6,057,547
4	(110.0, 50.0)	0.7° x 10.0 km (in) 1.3° x 20.0 km (out)	1,183	12,485	16,033	5,623,441	183,447	122,100	5,928,988
5	(80.0, 60.0)	0.2° x 10.0 km (in) 1.0° x 20.0 km (out)	1,028	12,555	19,288	6,006,788	197,460	131,146	6,335,394
6	(-70.0, 50.0)	0.1° x 5.0 km (in) 1.0° x 20.0 km (out)	2,469	12,565	17,167	5,658,950	178,360	127,522	5,964,832
7	(-120.0, 35.0)	0.1° x 5.0 km (in) 1.0° x 20.0 km (out)	3,618	12,612	19,817	6,190,973	206,735	134,798	6,532,506
8	(-170.0, 40.0)	0.3° x 10.0 km (in) 1.0° x 20.0 km (out)	705	12,659	19,515	6,448,371	209,746	134,384	6,792,501
9	(150.0, 35.0)	0.7° x 10.0 km (in) 1.3° x 20.0 km (out)	1,021	12,611	17,150	5,907,332	186,988	127,138	6,221,458
10	(60.0, 35.0)	0.3° x 10.0 km (in) 1.0° x 20.0 km (out)	2,307	12,551	19,120	5,974,579	198,425	131,238	6,304,242
11	(10.0, 40.0)	0.1° x 5.0 km (in) 1.0° x 20.0 km (out)	3,863	12,558	19,078	5,919,055	187,066	129,807	6,235,928
12	(-30.0, 35.0)	0.1° x 5.0 km (in) 1.0° x 20.0 km (out)	1,687	12,542	17,276	5,664,954	178,391	126,679	5,970,024

Table S2. Number of grid nodes at each depth which are arranged for conducting the tomographic inversion.

Grid depth (km) inside study region	Grid used outside study region	Number of nodes
15.0	o	23,453
32.5	-	13,955
50.0	o	23,325
75.0	-	13,744
100.0	o	22,917
140.0	-	13,491
180.0	o	22,270
220.0	-	13,095
260.0	o	21,811
300.0	-	12,817
340.0	o	21,191
380.0	-	12,438
420.0	o	20,686
460.0	-	12,169
500.0	o	20,039
575.0	-	11,723
650.0	o	19,027
725.0	-	11,114
800.0	o	18,005
875.0	-	10,519
950.0	o	17,185
1025.0	-	9,946
1100.0	o	16,257
1200.0	-	9,344
1300.0	o	15,027
1400.0	-	8,627
1500.0	o	13,837
1600.0	-	7,935
1700.0	o	12,703
1800.0	-	7,360
1900.0	o	11,738
2000.0	-	6,724
2100.0	o	10,693
2200.0	-	6,112
2300.0	o	9,695
2425.0	-	5,500
2550.0	o	8,523
2675.0	-	4,809
2800.0	o	7,551
Total		527,355

References

Amaru, M. L. (2007). Global travel time tomography with 3-D reference models. Doctoral thesis, Utrecht University. https://dspace.library.uu.nl/handle/1874/314949

Hosseini, K., Matthews, K. J., Sigloch, K., Shephard, G. E., Domeier, M., & Tsekhmistrenko, M. (2018), SubMachine: Web-Based tools for exploring seismic tomography and other models of Earth's deep interior. *Geochemistry, Geophysics, Geosystems*, 19(5), 1464-1483. https://doi.org/10.1029/2018GC007431

Kennett, B. L. N., & Engdahl, E. R. (1991). Traveltimes for global earthquake location and phase identification. *Geophysical Journal International*, 105, 429–465. https://doi.org/10.1111/j.1365-246X.1991.tb06724.x

Lu, C., Grand, S. P., Lai, H., & Garnero, E. J. (2019). TX2019slab: A new P and S tomography model incorporating subducting slabs. Journal of Geophysical Research: Solid Earth, 124, 11549–11567. https://doi.org/10.1029/2019JB017448

Ritsema, J., Deuss, A., van Heijst, H. J., & Woodhouse, J. H. (2011). S40RTS: a degree-40 shear-velocity model for the mantle from new Rayleigh wave dispersion, teleseismic traveltime and normal-mode splitting function measurements. Geophysical Journal International, 184, 1223–1236. https://doi.org/10.1111/j.1365-246X.2010.04884.x

Simmons, N. A., Forte, A. M., Boschi, V., & Grand, S. P. (2010). GyPSuM: A joint tomographic model of mantle density and seismic wave speeds. Journal of Geophysical Research: Solid Earth, 115(B12), B12310. https://doi.org/10.1029/2010JB007631

Simmons, N. A., Myers, S. C., Johannesson, G., & Matzel, E. (2012). LLNL-G3Dv3: Global P wave tomography model for improved regional and teleseismic travel time prediction. Journal of Geophysical Research: Solid Earth, 117, B10302. https://doi.org/10.1029/2012JB009525